3-25-2008

The Dynamics of Two Spherical Particles in a Confined Rotating Flow: Pedalling Motion

Karthik Mukundakrishnan
University of Pennsylvania, karthikm@seas.upenn.edu

Howard H. Hu
University of Pennsylvania, hhu@seas.upenn.edu

Portonovo S. Ayyaswamy
University of Pennsylvania, ayya@seas.upenn.edu

Recommended Citation

Mukundakrishnan, Karthik; Hu, Howard H.; and Ayyaswamy, Portonovo S., "The Dynamics of Two Spherical Particles in a Confined Rotating Flow: Pedalling Motion" (2008). *Departmental Papers (MEAM)*. 174.
http://repository.upenn.edu/meam_papers/174

Suggested Citation:
K. Mukundakrishnan, Howard: Howard H. Hu; and Portonovo Ayyaswamy. (2008). *The dynamics of two spherical particles in a confined rotating flow: pedalling motion. Journal of Fluid Mechanics* Vol. 599, March 2008. pp 169-204.

The Dynamics of Two Spherical Particles in a Confined Rotating Flow: Pedalling Motion

Abstract

We have numerically investigated the interaction dynamics between two rigid spherical particles moving in a fluid-filled cylinder that is rotating at a constant speed. The cylinder rotation is about a horizontal axis. The particle densities are less than that of the fluid. The numerical procedure employed to solve the mathematical formulation is based on a three-dimensional arbitrary Larangian–Eulerian (ALE), moving mesh finite-element technique, described in a frame of reference rotating with the cylinder. Results are obtained in the ranges of particle Reynolds number, $1<$<em>$\mathrm{Re}_{\mathrm{p}} \leq 60$, and shear Reynolds number, $1 \leq Re_s < 10$. Two identical particles, depending on initial conditions at release, approach each other ('drafting' and 'kissing'), tumble in the axial direction, and axially migrate towards opposing transverse planes on which they 'settle' (settling planes). Under some other initial conditions, the particles migrate directly onto their settling planes. For two identical particles, the settling planes are equidistant from the mid-transverse plane of the cylinder and the locations of the planes are determined by particle–particle and particle–wall force balances. Furthermore, for identical particles and given values of Re_p and Re_s, the locations of such settling planes remain the same, independent of the initial conditions at release. While located on these settling planes, as viewed in an inertial frame, the particles may attain three possible distinct states depending on the values of the Reynolds numbers. In one state (low Re_p, high Re_s), the particles attain and remain at fixed equilibrium points on their settling planes. In the second (all Re_p, low Re_s), they execute spiralling motions about fixed points on their respective settling planes. These fixed points coincide with the locations of the equilibrium point which would occur on the mid-axial plane in the case of a single particle. In the third state (low Re_p, moderate Re_s or high Re_p, moderate to high Re_s), they execute near-circular orbital motion on their respective settling planes, again about fixed points. These fixed points also coincide with the locations of the equilibrium points corresponding to single-particle dynamics. Both the spiral and near-circular motions of the particles occur in an out-of-phase manner with regard to their radial positions about the fixed point; the near-circular out-of-phase motion resembles bicycle pedalling. Also, in the second and third states, the particles simultaneously experience very weak axial oscillations about their settling planes, the frequency of such oscillations coinciding with the frequency of rotation of the circular cylinder. The behaviours of two non-identical particles (same density but different sizes, or same size but different densities) are different from those of identical particles. For example, non-identical particles may both end up settling on the mid-axial plane. This occurs when the locations of their corresponding single-particle equilibrium points are far apart. When such points are not far apart, particles may settle on planes that may not be symmetrical about the mid-axial plane. While located on their settling planes, their equilibrium states may not be similar. For example, for particles of the same density but of different sizes, the smaller of the two may execute a spiralling motion while the larger is in near-circular orbital motion. With particles of the same size but of different densities, while the lighter of the two approaches its equilibrium point on the mid-axial plane, the heavier one experiences a circular motion on the same plane about its equilibrium point. A major reason for the eventual attainment of these various states is noted to be the interplay between the particle–particle and particle–wall forces.

Disciplines

Engineering | Mechanical Engineering

Comments

Suggested Citation:
K. Mukundakrishnan, Howard: Howard H. Hu; and Portonovo Ayyaswamy. (2008). *The dynamics of two spherical particles in a confined rotating flow: pedalling motion. Journal of Fluid Mechanics* Vol. 599, March 2008. pp 169-204.

http://dx.doi.org/10.1017/S0022112007000092

J. Fluid Mech. (2008), *vol.* 599, *pp.* 169–204. © 2008 Cambridge University Press
doi:10.1017/S0022112007000092 Printed in the United Kingdom

The dynamics of two spherical particles in a confined rotating flow: pedalling motion

K. MUKUNDAKRISHNAN, HOWARD H. HU
AND P. S. AYYASWAMY†

Department of Mechanical Engineering and Applied Mechanics, 229, Towne Building, 220 S. 33rd Street, University of Pennsylvania, Philadelphia, PA 19104, USA

(Received 26 April 2007 and in revised form 13 November 2007)

We have numerically investigated the interaction dynamics between two rigid spherical particles moving in a fluid-filled cylinder that is rotating at a constant speed. The cylinder rotation is about a horizontal axis. The particle densities are less than that of the fluid. The numerical procedure employed to solve the mathematical formulation is based on a three-dimensional arbitrary Larangian–Eulerian (ALE), moving mesh finite-element technique, described in a frame of reference rotating with the cylinder. Results are obtained in the ranges of particle Reynolds number, $1 < Re_p \leqslant 60$, and shear Reynolds number, $1 \leqslant Re_s < 10$. Two identical particles, depending on initial conditions at release, approach each other (‘drafting’ and ‘kissing’), tumble in the axial direction, and axially migrate towards opposing transverse planes on which they ‘settle’ (settling planes). Under some other initial conditions, the particles migrate directly onto their settling planes. For two identical particles, the settling planes are equidistant from the mid-transverse plane of the cylinder and the locations of the planes are determined by particle–particle and particle–wall force balances. Furthermore, for identical particles and given values of Re_p and Re_s, the locations of such settling planes remain the same, independent of the initial conditions at release. While located on these settling planes, as viewed in an inertial frame, the particles may attain three possible distinct states depending on the values of the Reynolds numbers. In one state (low Re_p, high Re_s), the particles attain and remain at fixed equilibrium points on their settling planes. In the second (all Re_p, low Re_s), they execute spiralling motions about fixed points on their respective settling planes. These fixed points coincide with the locations of the equilibrium point which would occur on the mid-axial plane in the case of a single particle. In the third state (low Re_p, moderate Re_s or high Re_p, moderate to high Re_s), they execute near-circular orbital motion on their respective settling planes, again about fixed points. These fixed points also coincide with the locations of the equilibrium points corresponding to single-particle dynamics. Both the spiral and near-circular motions of the particles occur in an out-of-phase manner with regard to their radial positions about the fixed point; the near-circular out-of-phase motion resembles bicycle pedalling. Also, in the second and third states, the particles simultaneously experience very weak axial oscillations about their settling planes, the frequency of such oscillations coinciding with the frequency of rotation of the circular cylinder.

The behaviours of two non-identical particles (same density but different sizes, or same size but different densities) are different from those of identical particles. For example, non-identical particles may both end up settling on the mid-axial plane. This

---

† Author to whom correspondence should be addressed: ayya@seas.upenn.edu.

occurs when the locations of their corresponding single-particle equilibrium points are far apart. When such points are not far apart, particles may settle on planes that may not be symmetrical about the mid-axial plane. While located on their settling planes, their equilibrium states may not be similar. For example, for particles of the same density but of different sizes, the smaller of the two may execute a spiralling motion while the larger is in near-circular orbital motion. With particles of the same size but of different densities, while the lighter of the two approaches its equilibrium point on the mid-axial plane, the heavier one experiences a circular motion on the same plane about its equilibrium point. A major reason for the eventual attainment of these various states is noted to be the interplay between the particle–particle and particle–wall forces.

1. Introduction

Particulate-laden rotating flows occur in a variety of applications such as in technology related to colloidal suspensions, biotechnologies employing rotating-wall bioreactors, and in sedimentation processes. Such flows have also been employed in diverse applications related to tissue growth engineering and fundamental cell biology studies. The reactors in such studies generally consist of a thin cylinder rotating about its horizontal axis, completely filled with the liquid culture medium. Spherical microcarrier particles constitute the dispersed medium. NASA-designed rotating wall bioreactors belong to this category. A discussion of rotating-wall bioreactors is provided in Ayyaswamy & Mukundakrishnan (2007). Studying the effectiveness of such bioreactors requires an understanding of the mechanics of the flow and the stresses caused by the flow on microcarriers on whose surfaces cells are grown. Factors that affect the motions of these microcarriers, such as the viscosity of the fluid, the size of the microcarriers, the density of the microcarrier material, and the rotation rate of the bioreactor, are all important parameters in the accurate determination of strategies for better culturing with increased suspension periods. Knowledge of the flow field is also necessary to ascertain mass transport between the culture medium and cells, and the stresses acting on the microcarriers or cells (Gao, Ayyaswamy & Ducheyne 1997; Mukundakrishnan 2005; Lynch *et al.* 2006; Ayyaswamy & Mukundakrishnan 2007).

Many numerical studies of single-particle dynamics in rotating flows have been concerned with the motion of a particle in a fluid-filled cylinder rotating about a vertical axis (Minkov, Ungarish & Israeli 2000, 2002; Wang, Lu & Zhuang 2004). Fewer studies exist on the single-particle dynamics in a fluid-filled cylinder rotating about a horizontal axis (see figure 1), (see for example, Annamalai & Cole 1986; Roberts, Kornfeld & Fowlis 1991; Gao *et al.* 1997; Coimbra & Kobayashi 2002; Lee & Ladd 2002; Ramirez *et al.* 2004). Most of the latter studies have employed a modified form of Maxey-Riley equation (Maxey & Riley 1982; Michaelides 2003) to track the particle motion. Coimbra & Kobayashi (2002) have examined the role of lift forces and have provided explicit expressions for various forces. Bagchi & Balachandar (2002) have investigated the problem of a rigid sphere situated in an ambient flow of solid-body rotation by employing direct numerical simulations (DNS), and have shown that the lift coefficient is enhanced compared to that in linear shear flow. A majority of the numerical studies cited above have considered only single-particle dynamics in an infinite fluid medium. Our study considers the dynamics of

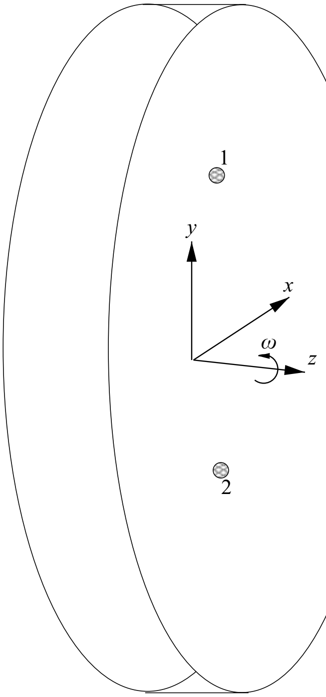

FIGURE 1. Schematic of the rotating wall vessel with 2 particles. z axis is the axis of rotation and the transverse plane is the $x-y$ axis in a rotating frame. 1 and 2 denote the two spherical particles, respectively.

two particles in a finite fluid-filled rotating cylinder. This is therefore an obvious and appropriate extension for understanding particle behaviour in bioreactors.

Recent experiments on rotating flows with multiple particles have shown interesting flow features. Mullin *et al.* (2005) have presented experimental results for the motion of one, two and three solid heavier-than-fluid (HTF) spheres that were free to move in a fluid-filled cylinder rotating about a horizontal axis. For the two-particle system, the motion of the particles was noted to be periodic, and for a certain range of Reynolds numbers, the two particles were equally spaced on either side of the mid-axial plane and oscillated in an anti-phase manner. Three-particle systems exhibited persistent low-dimensional chaos. It is stated that the nonlinear behaviours noted arise because of particle–particle and particle–wall interactions. In experiments with larger numbers of spherical particles, Lipson (2001) and Matson, Ackerson & Tong (2003) have observed number density fluctuations along the horizontal axis. Buoyant particles (negatively, neutrally and positively buoyant) are shown to display axial banding. Seiden, Lipson & Franklin (2004) have explained the banding phenomenon as arising from the excitation of inertial standing waves in the rotating fluid.

In the present study, we have numerically investigated the motion of two lighter-than-fluid (LTF) spherical particles in a fluid-filled cylinder rotating about a horizontal axis by DNS. DNS techniques have been demonstrated to be powerful tools in capturing the detailed interparticle and particle–wall interactions in rectilinear flows (Hu 1996; Hu, Patankar & Zhu 2001; Swaminathan, Mukundakrishnan & Hu 2006). These studies have employed an arbitrary Lagrangian–Eulerian (ALE) scheme, coupled with a body-fitted moving finite-element mesh in an inertial frame of reference.

In the present study, ALE has been formulated in a non-inertial rotating frame of reference. This choice of the reference frame has been shown to be the most convenient one for analysing particulate-laden rotating flows (Mukundakrishnan 2005).

Our simulations have revealed several fascinating features with regard to two-particle motion. New states of equilibrium have been realized. In this paper, we will concentrate on describing the new phenomena revealed by our numerical studies.

The present paper is organized as follows. Section 2 describes the mathematical formulation of the governing equations of motion in a rotating frame of reference, followed by a brief discussion of the numerical methodology in § 3. Section 4 provides results for validating our numerical procedure. Detailed results of binary particle interactions in rotating flows are described in § 5 for identical particles and in § 6 for non-identical particles, followed by conclusions in § 7.

2. Mathematical formulation

2.1. *Rotating frame formulation*

The fluid and particle equations as formulated in a rotating frame of reference will now be described. In a frame of reference with its origin coinciding with the centre of the cylinder and rotating with a constant angular velocity $\boldsymbol{\omega} = \omega\hat{\boldsymbol{k}}$, where $\hat{\boldsymbol{k}}$ is the unit vector along the horizontal rotation axis (z-axis, see figure 1), the fluid motion satisfies the conservation of mass,

$$\nabla \cdot \boldsymbol{u} = 0, \tag{1}$$

and the conservation of momentum,

$$\rho_f \left(\frac{\partial \boldsymbol{u}}{\partial t} + \boldsymbol{u} \cdot \nabla \boldsymbol{u} + 2\,\boldsymbol{\omega} \times \boldsymbol{u} + \boldsymbol{\omega} \times (\boldsymbol{\omega} \times \boldsymbol{x}) \right) = \rho_f \boldsymbol{g} + \nabla \cdot [-P\boldsymbol{I} + \mu_f [\nabla \boldsymbol{u} + (\nabla \boldsymbol{u})^T]]. \tag{2}$$

Here, $\boldsymbol{u}$ is the fluid velocity vector measured in the rotating frame, ρ_f is the density, μ_f is the viscosity, subscript f denotes fluid, $\boldsymbol{g}$ is the acceleration due to gravity vector, P is the total pressure and $\boldsymbol{x}$ $(= x\boldsymbol{i} + y\hat{\boldsymbol{j}} + z\hat{\boldsymbol{k}})$ is the position vector in the fluid. The third term on the left-hand side of the momentum equation denotes the Coriolis force and the fourth term denotes the centrifugal force. The pressure P can be combined with the gravity and centrifugal force terms to give a reduced dynamic pressure, p, given by,

$$p = P - \rho_f(\boldsymbol{g} \cdot \boldsymbol{x}) + \tfrac{1}{2}\rho_f(\boldsymbol{\omega} \times \boldsymbol{x}) \cdot (\boldsymbol{\omega} \times \boldsymbol{x}), \tag{3}$$

where the relation $\boldsymbol{\omega} \times \boldsymbol{\omega} \times \boldsymbol{x} = \frac{1}{2}\nabla[(\boldsymbol{\omega} \times \boldsymbol{x}) \cdot (\boldsymbol{\omega} \times \boldsymbol{x})]$ has been used. The momentum equation becomes:

$$\rho_f \left(\frac{\partial \boldsymbol{u}}{\partial t} + \boldsymbol{u} \cdot \nabla \boldsymbol{u} + 2\,\boldsymbol{\omega} \times \boldsymbol{u} \right) = \nabla \cdot [-p\boldsymbol{I} + \mu_f [\nabla \boldsymbol{u} + (\nabla \boldsymbol{u})^T]]. \tag{4}$$

Next, consider the equations governing the particle motion. For the ith particle, the modified Newton's equation for the translational part of the motion is given by (see Mukundakrishnan (2005) for details):

$$m_i \left(\frac{\mathrm{d}\boldsymbol{U}_i}{\mathrm{d}t} + 2\,\boldsymbol{\omega} \times \boldsymbol{U}_i \right) = \boldsymbol{F}_i + \boldsymbol{G}_i, \tag{5}$$

$$\frac{\mathrm{d}\boldsymbol{X}_i}{\mathrm{d}t} = \boldsymbol{U}_i, \tag{6}$$

where m_i is the mass of the ith particle, $\boldsymbol{U}_i$ is the velocity of the particle, $\boldsymbol{F}_i$ is the hydrodynamic force exerted by the fluid on the particle, $\boldsymbol{G}_i$ is the body force and $\boldsymbol{X}_i$

is the position of the centroid of the ith particle. Here, $\boldsymbol{F}_i$, $\boldsymbol{G}_i$ are given by:

$$\boldsymbol{F}_i = \int_{\partial \Gamma_i} [-p\boldsymbol{I} + \mu_f[\nabla \boldsymbol{u} + (\nabla \boldsymbol{u})^T]] \cdot \hat{\boldsymbol{n}} \, \mathrm{d}S, \tag{7}$$

$$\boldsymbol{G}_i = (m_i - m_f)[\boldsymbol{g} - \omega^2 \boldsymbol{x}], \tag{8}$$

where $\hat{\boldsymbol{n}}$ is the outward normal to the surface $\partial \Gamma_i$ of the ith particle, $\mathrm{d}S$ is an elemental surface area, and m_f is the mass of fluid.

Now consider, the rotational part of the motion for the ith spherical particle, in a reference frame fixed to its centre of mass (a body-fixed frame) and rotating with the constant angular velocity, ω, of the fluid. This is described by the Euler equation. It may be noted that for a spherical particle, a co-rotating frame coincides with the principal axis. This is a convenient frame to describe the Euler equation, since the rotational velocity components may now be described in the same frame as the translational velocity components, therefore involving no additional coordinate transformations. The Euler equations, in the body-fixed frame, governing the rotational motion are:

$$\frac{\mathrm{d}(\boldsymbol{I}_i \boldsymbol{\Omega}_i)}{\mathrm{d}t} + \boldsymbol{\omega} \times \boldsymbol{I}_i \boldsymbol{\Omega}_i = \boldsymbol{C}_i, \tag{9}$$

$$\frac{\mathrm{d}\boldsymbol{\Theta}_i}{\mathrm{d}t} = \boldsymbol{\Omega}_i, \tag{10}$$

where $\boldsymbol{I}_i$ is the moment of inertia tensor, $\boldsymbol{\Omega}_i$ is the angular velocity of the ith particle with respect to the fluid in the rotational frame, $\boldsymbol{C}_i$, is the hydrodynamic moment vector, and $\boldsymbol{\Theta}_i$ is the angular position of the particle. $\boldsymbol{C}_i$ is given by:

$$\boldsymbol{C}_i = \int_{\partial \Gamma_i} (\boldsymbol{x} - \boldsymbol{X}_i) \times [(-p\boldsymbol{I} + \mu_f[\nabla \boldsymbol{u} + (\nabla \boldsymbol{u})^T]) \cdot \hat{\boldsymbol{n}}] \, \mathrm{d}S, \tag{11}$$

where $\boldsymbol{x}$ is the position vector of a point on the surface of the ith particle from the origin of the cylinder.

The initial conditions for the problem are:

$$\boldsymbol{u}(t = 0) = 0, \tag{12}$$

$$\boldsymbol{U}_i(t = 0) = 0, \tag{13}$$

$$\boldsymbol{\Omega}_i(t = 0) = -\boldsymbol{\omega}. \tag{14}$$

The boundary conditions are:

$$\boldsymbol{u} = \boldsymbol{0} \text{ on cylinder walls } \partial \Gamma_{ar}, \tag{15}$$

$$\boldsymbol{u} = \boldsymbol{U}_i + \boldsymbol{\Omega}_i \times (\boldsymbol{x} - \boldsymbol{X}_i) \text{ on particle surface } \partial \Gamma_i. \tag{16}$$

We solve the governing equations (1), (4–6), (9) and (10) together with the initial and boundary conditions given by equations (12)–(16) for the flow field, and the trajectory of the particles.

For the results reported in this paper, the distance between the sidewalls of the fluid-filled cylinder is fixed at $16a$, while its radius is $100a$. Here, a denotes the radius of the particle where the sizes are the same, and the radius of the smaller particle where the sizes are different. These dimensions have been selected on the basis of extensive numerical experimentation and are such that the radial wall has negligible influence on particle dynamics.

3. Numerical methodology

In the fluid–particle system, owing to the complex and irregular nature of the domain occupied by the fluid, finite-element techniques are particularly powerful for discretizing the governing fluid equations. In order to use the finite-element method, we first seek a weak formulation that incorporates both the fluid and particle equations, namely equations (4), (5), (9). The details of the weak formulation for the rotating frame are given in Mukundakrishnan (2005). The domain movement is handled by an arbitrary Lagrangian–Eulerian (ALE) scheme. The details of spatial discretization, mesh generation, mesh movement techniques, and temporal discretization of time derivatives follow procedures discussed in Hu *et al.* (2001). These details will not be repeated here. Briefly, the fluid domain is approximated by quadratic tetrahedral finite-elements (10 nodes defined per tetrahedron with 10 basis functions that are second-order polynomials). The discrete solution for the fluid velocity is approximated by piecewise quadratic functions (P2 elements), and is assumed to be continuous over the domain. The discrete solution for the pressure is taken to be piecewise linear and continuous (P1 element) consistent with the Ladyzhenskaya–Babuska–Brezzi (LBB) or inf-sup condition. This yields convergent solutions. A second-order implicit time-stepping scheme is used for all the calculations.

For all the results reported in this paper excepting that in figure 4(*a*), we have employed the rotating-frame formulation. Some of the major advantages of a rotating-frame formulation are as follows.

(i) Since the background flow is subtracted out, this scheme offers significant simplicity for computing particle motion at various Re_s. For example, for low Re_p and low Re_s (see § 3.1 for the definitions for Re_p and Re_s) or for high Re_p with moderate to high Re_s, the rotating-frame computations enable the use of a time step an order of magnitude higher for achieving the same accuracy as with an inertial frame. Details of such comparisons, however, are not included here (see Mukundakrishnan 2005).

(ii) It is also easier to handle the body force term (second term on the right-hand side of (8)) that arises owing to the manifestation of pressure associated with rigid-body motion of the background fluid. Furthermore, there is a reduction of the error in computing the total force acting on the particle. As a consequence, the trajectories are determined more accurately.

Although the rotating frame formulation has been employed in computations, we have chosen to present most of the results for particle positions as viewed in an inertial frame. This inertial frame is denoted by x_i, y_i, z_i coordinate axes for easy comprehension of the results. The transformation of the rotating frame results (x, y, z) for the particle position to the inertial frame (x_i, y_i, z_i) has been effected using the following relationships:

$$x_i = x\cos(\omega t) - y\sin(\omega t), \tag{17a}$$

$$y_i = x\sin(\omega t) + y\cos(\omega t), \tag{17b}$$

$$z_i = z. \tag{17c}$$

The negative y_i-axis coincides with the direction of gravity vector. The variables z_i and z are used interchangeably in the text since they are the same in both reference frames. It must be emphasized that the feature of expressing the results obtained in a rotating frame as viewed in an inertial frame is clearly different from generating the results employing an inertial frame formulation. An inertial frame formulation has also been used in this study purely for validation purposes (see § 4).

3.1. *Non-dimensionalization aspects*

In order to non-dimensionalize the equations, the following scales are chosen. The particle diameter $2a$, where a is the particle radius, is the characteristic length scale, the gravitational slip velocity of the particle U_{slip}, is the characteristic velocity scale, $2a/U_{slip}$ is the time scale, the cylinder rotation rate ω is the characteristic rotational speed of the particle, and $\rho_f U_{slip}^2$ is the pressure scale is the pressure scale. The magnitude of U_{slip} may be estimated by balancing fluid drag with the effective (net) weight of the particle, $(\rho_f - \rho_f)V_p g$, where V_p is the volume of the spherical particle. This yields, $U_{slip} \sim O(2|\Delta\rho|a^2 g/9\mu_f)$, where $|\Delta\rho|$ is the magnitude of the density difference between the fluid and the particle. With, $\nabla = \hat{\nabla}/(2a)$, $\boldsymbol{u} = U_{slip}\hat{\boldsymbol{u}}$, $t = (2a/U_{slip})\hat{t}$, $p = \rho_f U_{slip}^2 \hat{p}$, equations (1) and (4) (after omitting superscripts $\hat{()}$ for the non-dimensional quantities) become:

$$\nabla \cdot \boldsymbol{u} = 0, \tag{18}$$

$$Re_p\left(\frac{\partial \boldsymbol{u}}{\partial t} + (\boldsymbol{u}\cdot\nabla)\boldsymbol{u}\right) + Re_s\,(2\hat{\boldsymbol{k}} \times \boldsymbol{u}) = -Re_p \nabla p + \nabla \cdot [\nabla \boldsymbol{u} + (\nabla \boldsymbol{u})^T], \tag{19}$$

where

$$Re_p = \frac{2aU_{slip}}{\nu_f} = \frac{4}{9}\frac{a^3(1-\rho_p/\rho_f)g}{\nu_f{}^2}$$

is the particle Reynolds number based on a characteristic gravitational slip velocity, and $Re_s = \boldsymbol{\omega}(2a)^2/\nu_f$ is the shear Reynolds number. It can be noted that, for a given particle size a and fluid viscosity ν_f, Re_p emphasizes the role of the density ratio ρ_p/ρ_f, while Re_s highlights the role of the cylinder rotation rate ω.

For particle translation, the non-dimensional form of (5), after some algebraic manipulation, becomes:

$$\begin{aligned} &\frac{\rho_p}{\rho_f}\left[Re_p\frac{\mathrm{d}\boldsymbol{U}_i}{\mathrm{d}t} + Re_s(2\hat{\boldsymbol{k}} \times \boldsymbol{U}_i)\right] \\ &\quad = \left(1 - \frac{\rho_p}{\rho_f}\right)\frac{Re_s{}^2}{Re_p} r(\cos\theta\hat{\boldsymbol{e}}_x + \sin\theta\hat{\boldsymbol{e}}_y) + 18(\sin\theta\hat{\boldsymbol{e}}_x + \cos\theta\hat{\boldsymbol{e}}_y) \\ &\qquad + \frac{6}{\pi}\int_{\Gamma_i}[Re_p(-p\boldsymbol{I}) + (\nabla\boldsymbol{u} + (\nabla\boldsymbol{u})^T)]\cdot\hat{\boldsymbol{n}}\,\mathrm{d}\Gamma_i, \end{aligned} \tag{20}$$

where r is the non-dimensional radial position of the particle ($r = \sqrt{x^2 + y^2} = \sqrt{x_i{}^2 + y_i{}^2}$), and $\hat{\boldsymbol{e}}_x$, $\hat{\boldsymbol{e}}_y$ are the unit vectors in the transverse plane along the x and y directions, respectively. Also, $\theta = \tan^{-1}(y/x)$, is the angular position of the particle in the transverse plane of the cylinder, and (x, y) denotes the location of particle on the transverse (axial) plane. For particle rotation, with $\hat{\boldsymbol{\Omega}}_i = \boldsymbol{\Omega}_i/\boldsymbol{\omega}$, the non-dimensional form of equation (9) (after dropping superscripts) is given by:

$$\frac{\rho_p}{\rho_f}Re_s\frac{\mathrm{d}\boldsymbol{\Omega}_i}{\mathrm{d}t} + \frac{\rho_p}{\rho_f}\frac{Re_s{}^2}{Re_p}(\hat{\boldsymbol{k}} \times \boldsymbol{\Omega}_i) = \frac{60}{\pi}\int_{\partial\Gamma_i}(\boldsymbol{x} - \boldsymbol{X}_i) \times [Re_p(-p\boldsymbol{I}) + (\nabla\boldsymbol{u} + (\nabla\boldsymbol{u})^T)]\cdot\hat{\boldsymbol{n}}\,\mathrm{d}\Gamma_i. \tag{21}$$

The non-dimensional initial conditions for the problem are:

$$\boldsymbol{u}(t = 0) = 0, \tag{22}$$

$$\boldsymbol{U}_i(t = 0) = 0, \tag{23}$$

$$\boldsymbol{\Omega}_i(t = 0) = -1. \tag{24}$$

The non-dimensional boundary conditions for the rotating flow problem are:

$$\boldsymbol{u} = \boldsymbol{0} \quad \text{on} \ \partial\Gamma_w, \tag{25}$$

$$\boldsymbol{u} = \boldsymbol{U}_i + \frac{Re_s}{Re_p}\hat{\boldsymbol{k}} \times (\boldsymbol{x} - \boldsymbol{X}_i) \quad \text{on} \ \partial\Gamma_i. \tag{26}$$

However, for all the numerical results presented in this study, time is normalized by the rotation period of the cylinder. This non-dimensional time is $t^* = t/(2\pi/\omega)$.

4. Validation of the numerical procedure

The numerical code is validated in two ways. (i) By evaluating the motion of a single particle in a fluid-filled cylinder rotating about a horizontal axis. The solution obtained will be examined to verify conformity with trends predicted by other existing solutions. (ii) By comparison of the solutions to the two particle problem obtained by employing two different frames of reference in the problem formulation, namely, the inertial and rotational frames of reference.

With regard to the existing numerical/analytical studies of a single particle motion (Annamalai & Cole 1986; Roberts *et al.* 1991; Gao *et al.* 1997; Coimbra & Kobayashi 2002; Lee & Ladd 2002; Ramirez *et al.* 2004), most have employed the Maxey–Riley equation:

$$\rho_p V_p \frac{\mathrm{d}\boldsymbol{U}_p}{\mathrm{d}t} + C_{\mathrm{v}}\rho_f V_p \left(\frac{\mathrm{d}\boldsymbol{U}_p}{\mathrm{d}t} - \frac{\mathrm{D}\boldsymbol{U}_f}{\mathrm{D}t}\right) = -V_p\nabla p + (\rho_p - \rho_f)V_p\boldsymbol{g} + \boldsymbol{F}_D + \boldsymbol{F}_L, \tag{27}$$

where $\mathrm{D}/\mathrm{D}t$ is the substantial derivative following the motion of fluid and $\mathrm{d}/\mathrm{d}t$ is the total derivative following the spherical particle. Here, $\boldsymbol{U}_p$, $\boldsymbol{U}_f$ $(= \boldsymbol{\omega} \times \boldsymbol{r})$, C_{v}, $\boldsymbol{F}_D$ and $\boldsymbol{F}_L$ denote the velocities of the particle and of the fluid, the added mass coefficient (=0.5 for a rigid spherical particle), the drag acting on the particle, and the hydrodynamic lift and other history forces.

When considered in the context of a single lighter-than-fuid spherical particle motion in an unbounded rotating flow, the solution to (27) shows that the particle eventually attains a fixed equilibrium state. This equilibrium state as observed in an inertial frame is charactertized by an equilibrium point whose location may be denoted by x_i and y_i coordinates on the transverse plane. Many studies of this equation have not considered the lift or the history forces (see, for example Gao *et al.* 1997), and have described the coordinates of the fixed equilibrium state. Coimbra & Kobayashi (2002) analysed the equation with the inclusion of lift and history forces, but for very low values of Re_p and Re_s. They affirm the existence of a fixed equilibrium point and conclude that the inclusion of additional forces in the analysis may not significantly change the value of the x_i-coordinate but the value of the y_i-coordinate is altered. In particular, the presence of lift forces has been stated to be important in determining the final coordinates.

We will validate our numerical procedure by studying the motion of a single particle employing DNS (see equations (1)–(16)), and finding the final equilibrium state. The following parameters are considered: $\rho_p/\rho_f = 0.8$, $Re_p = 56$ and $Re_s = 3$. These are representative of particle parameters in bioreactor studies. Our computations show that the particle eventually attains a stable fixed equilibrium state whose coordinate locations are given by $x_i/2a = -7.7$, $y_i/2a = 0.03$. We have also solved (27) without the inclusion of lift and history forces. For $\boldsymbol{F}_D$, we use the Schiller–Naumann correlation (Schiller & Nauman 1933). The predicted coordinates of the fixed equilibrium point are $x_i/2a = -7.86$, $y_i/2a = 0.85$. It may be noted that the x_i coordinates predicted by

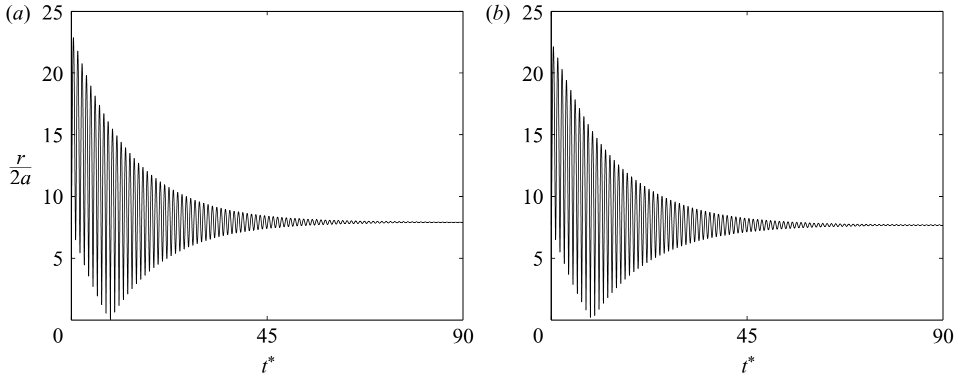

FIGURE 2. Comparison of radial position histories between (*b*) DNS and (*a*) the solution of (27) without the inclusion of lift and history forces. The parameters are: $\rho_p/\rho_f = 0.8$, $Re_p = 56$ and $Re_s = 3$. (*a*) Final fixed equilibrium point position is given by $x_i/2a = -7.86$, $y_i/2a = 0.85$. (*b*) Final fixed equilibrium point position is given by $x_i/2a = -7.7$, $y_i/2a = 0.03$.

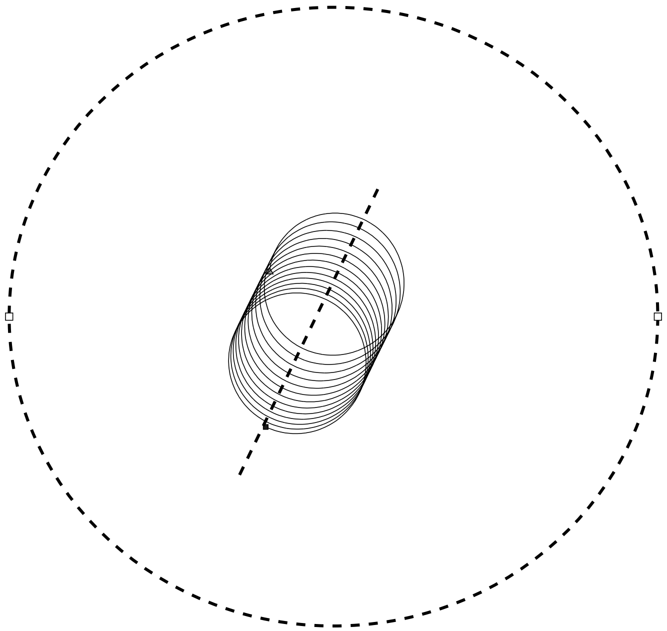

FIGURE 3. A typical epitrochoid trajectory of the particle as viewed in the rotating frame of reference for the case of single-particle dynamics. The dashed line circle represents the enclosing cylinder. The straight dashed line is the locus of the instantaneous centre of the epitrochoidal trajectory.

DNS and by the solution of (27) not including lift or history forces, are essentially the same. However, the y coordinates are significantly different, the DNS confirming the trend of lowering the value of y_i coordinate if all the forces are properly accounted for (Coimbra & Kobayashi 2002). In figure 2, we display the radial positions of the particle in its trajectory as a function of time. Both the results predict similar decay rate for the radial position culminating in a fixed equilibrium point. Figure 3 shows the trajectory of the particle in a rotating frame of reference. As viewed in this frame, the particle describes a transient two-dimensional helix or epitrochoidal-like

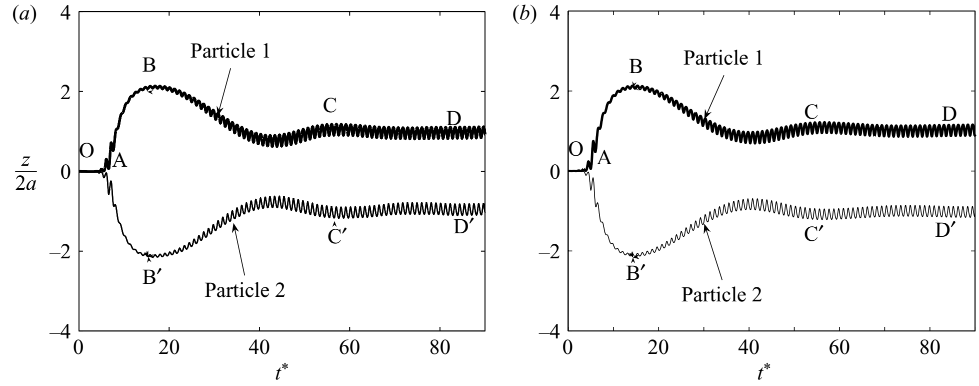

FIGURE 4. Validation of the numerical code using solutions obtained in two different reference frames. (*a*) Inertial frame; (*b*) rotating frame. Only the axial migration history is shown for elucidation purposes. The parameters are: $\rho_f = 1.0\,\mathrm{g\,cm^{-3}}$, $\mu_f = 0.01\,\mathrm{g\,cm^{-1}\,s^{-1}}$, $\rho_p = 0.99\,\mathrm{g\,cm^{-3}}$, $\omega = 15\,\mathrm{r.p.m.}$, $a = 400\,\mu\mathrm{m}$. These correspond to $\rho_p/\rho_f = 0.99$, $Re_p = 2.8$ and $Re_s = 1.0$.

trajectory in a clockwise manner eventually culminating in a circle of fixed radius. Each circular orbit seen in the trajectory represents approximately one rotation cycle of the particle motion. The locus of the instantaneous centre of the helical trajectory of a single particle is seen to follow a straight line (dotted lines in Figure 3).

For $\rho_p/\rho_f = 0.001$, $Re_p = 0.1$ and $Re_s = 0.2$ (*Re* based on our definitions), Coimbra & Kobayashi (2002) give $x_i/a = -0.98$ and $y_i/a = -0.09$. These would compare with DNS predictions of $x_i/a = -0.83$ and $y_i/a = -0.03$. It must be remembered that the DNS results are for particle motion in a rotating flow confined within a cylinder. The predicted trends are noted to be the same.

We now offer another validation of our numerical code by comparing results obtained using formulations in two separate reference frames – inertial and rotating frames. This comparison will be made in the context of two particles in motion. Referring to figure 4, at $t^* = 0$, two identical particles are released close to each other on the mid-transverse plane of the rotating cylinder (on the (x, y) plane at $z = 0$), denoted by O. The points of release are located on either side of the negative x-axis slightly above and below a point that is two particle diameters away from the origin (see figure 1). The particles approach each other and tumble axially (point A). Subsequent to this, the particles migrate axially in opposite directions towards the lateral walls. At B, B′, wall repulsion makes the particles migrate inwards towards the mid-transverse plane. Eventually, a balance is attained between the particle–particle repulsive forces and the particle–wall repulsive forces. The particles settle on two distinct transverse planes that are symmetrically located about the mid-transverse plane (point C, C′). The predictions as computed from inertial and rotating-frame formulations are found to be identical and serve to validate the code.

5. Detailed study of two particle interaction dynamics

In this section, the detailed dynamics of interaction between two identical lighter-than-fluid particles is presented and discussed. The ranges of Re_p and Re_s investigated are $1 < Re_p \leqslant 60$ and $1 \leqslant Re_s < 10$. For the ranges studied, the following features are noted.

Particles released on the same transverse plane of the rotating cylinder

(*a*) Two particles released on the mid-transverse plane, in close proximity (see figure 5*a*), say, the interparticle gap at release is of the order of a few particle diameters, are noted to approach each other ('drafting'), stay for a short time as neighbours ('kissing'), and this is followed by 'tumbling' along the axial direction. Numerical simulations show that an interparticle separation distance of about three particle diameters may be regarded as 'close proximity' release. On the other hand, if the two particles were to be released widely separated from each other, each particle would attempt to move towards the equilibrium point that is characteristic of a single particle (drafting). They become neighbours in the vicinity of this equilibrium point ('kissing'), and this is followed by tumbling (see figure 5*b*). Subsequent to tumbling, the particles migrate along axial directions towards lateral walls while continuing motion on transverse planes. Eventually, they 'settle' on transverse planes that are equidistant apart from the mid-transverse plane of the cylinder. This settling (transverse) plane denotes the plane at which equilibrium has been attained between particle–particle and particle–wall forces in the axial direction.

(*b*) Two particles on the same transverse plane different from the mid-transverse plane exhibit two different types of behaviour depending on the proximity of particles at release.

(i) If the particles are initially very close to each other (a gap less than or equal to one particle diameter) (see figure 5*c*, *d*), then they are noted to draft, kiss, and tumble during a short time and axially migrate. Eventually, they settle on transverse planes that are equidistant from the mid-transverse plane. The locations of settling planes are determined by interparticle and particle–wall force balances in the axial direction.

(ii) If the particles are initially widely separated (see figure 5*e*), then they first axially migrate to the mid-transverse plane, and their subsequent history follows that described earlier in item (*a*) for figure 5(*b*).

While located on settling planes, for items (*a*) and (*b*), the particles individually experience three possible 'stable states' which will be subsequently discussed.

Particles released on two different transverse planes of the rotating cylinder

(*a*) If the particles are initially widely separated (see figure 5*f*), they first axially migrate to the mid-transverse plane and their subsequent history follows that described earlier under item 1 for figure 5(*b*) of the previous classification ('Particles released on the same transverse plane of the rotating cylinder'). For this case, the particle–wall forces overwhelm particle–particle interaction forces. As a result, they first migrate to the mid-transverse plane.

(*b*) When the initial separation distance between the particles, as projected on the (x, y)-plane, δ, is less than a particle diameter (see figure 5*g*–*i*), then the particles do not undergo the regimes of drafting, kissing and tumbling. Instead, they axially migrate directly and settle on transverse planes that are equidistant from the mid-plane. This is because, for such small separation distances (as projected on the transverse plane), the particle–particle repulsive forces along the axial direction becomes comparable to that of the particle–wall interaction forces. The particles do not reach the mid-transverse plane. The locations of the settling planes are determined by interparticle and particle–wall force balances in the axial direction.

Herein again, while located on settling planes, the particles individually experience three possible 'stable states' which will be subsequently discussed.

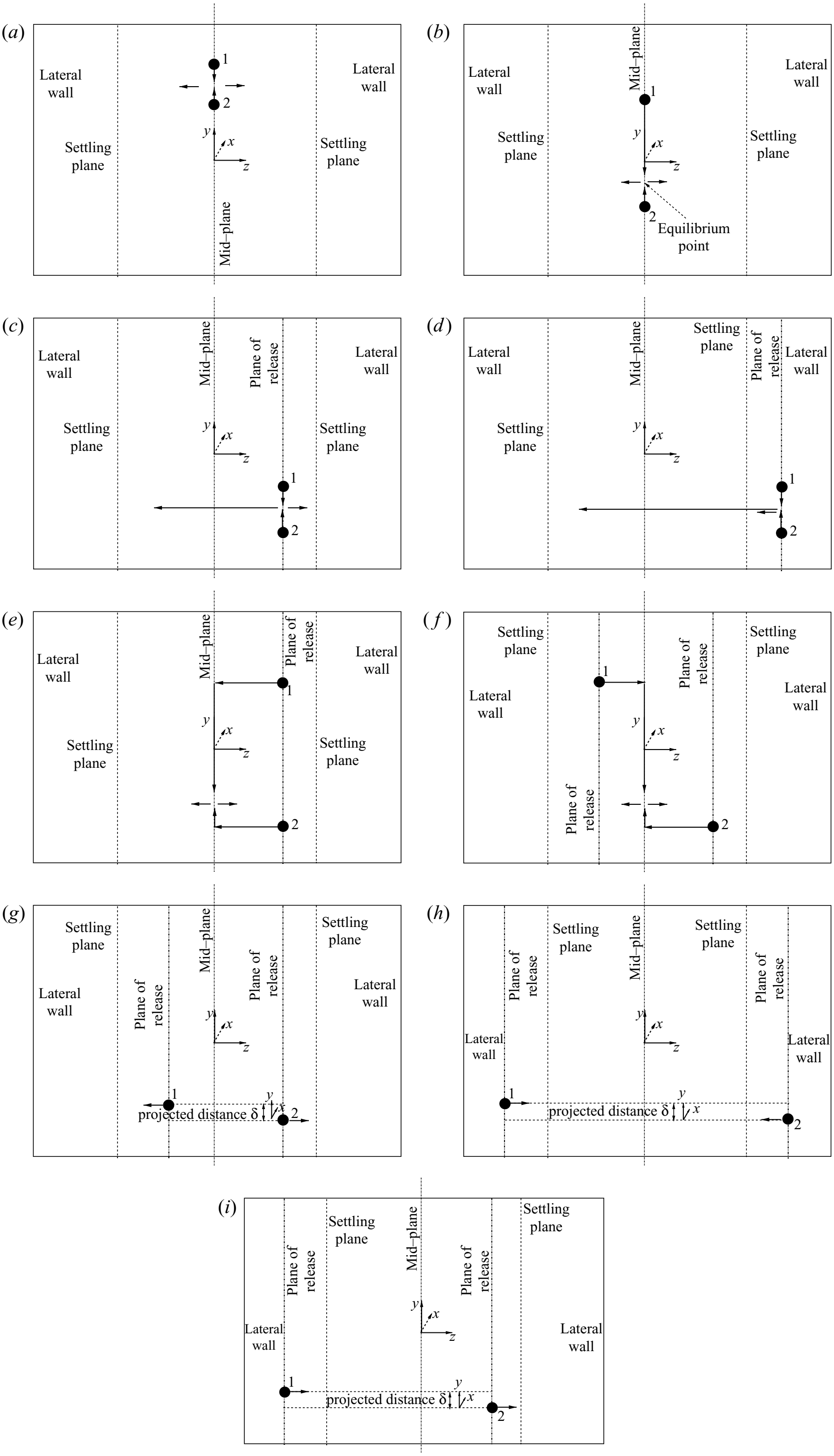

FIGURE 5. Various locations of release of particles.

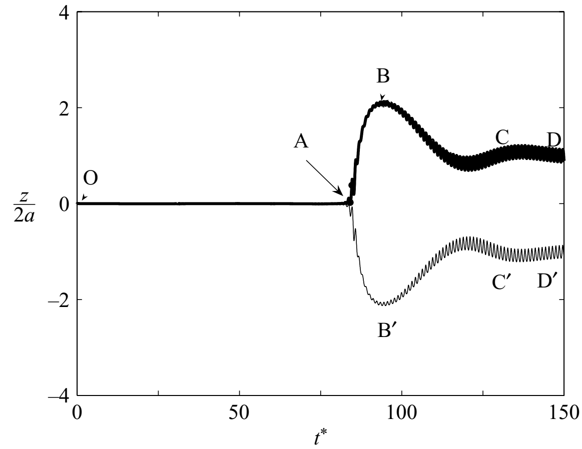

FIGURE 6. Axial migration of two particles released from positions shown in figure 5(*b*). The parameters of the problem are the same as given in figure 4.

The major mechanism proposed in the present study for the novel features described above is the wake interaction dynamics of particles coupled with wall effects. The wake interaction dynamics is described in detail in the following sections.

A typical case for $\rho_p/\rho_f = 0.99$, $Re_p \approx 2.8$ and $Re_s \approx 1.0$ will now be discussed to elucidate the major mechanisms governing the two-particle interaction dynamics. This combination of Reynolds numbers brings into prominence the role of all the terms in the momentum equation.

5.1. *Detailed discussion of drafting, kissing, tumbling and axial migration*

To highlight these various features of two-particle dynamics, we focus on particles released on the mid-axial (mid-transverse) plane of the cylinder.

5.1.1. *Drafting*

Particles released at arbitrary locations far away from each other on the mid-transverse plane, each start moving in a single-particle fashion towards the same equilibrium fixed point that is characteristic of single-particle dynamics (see discussions on single-particle dynamics under validation in § 4). The equilibrium point is located on this same (mid-axial) plane. Such motion brings the particles closer to each other in the vicinity of the equilibrium point and the wake interaction between the particles controls the subsequent dynamics. On the other hand, if two particles are released on the mid-transverse plane and in close proximity to each other, but away from the equilibrium location of a single particle, they approach each other (figure 5*a*). This approach of one particle towards the other corresponds to drafting in rotating flows. In figure 4(*a*), drafting is seen to occur during O–A. If the particles are not in close proximity to each other when released on the mid-transverse plane, they approach each other as shown in figure 6 except now, the drafting period is longer. This is as expected. Now, with regard to Figure 5(*b*), where the two particles are released in mid-plane far apart from each other and one on either side of the equilibrium point, the particles again draft and approach the equilibrium point before tumbling occurs from that location. In that case, point A in figure 6 would be the same as the equilibrium point. Drafting results in the reduction of the interparticle gap as a function of time and this is evident from figure 7. In this figure, the variation in the normalized interparticle gap (ℓ) is displayed as a function of time when the particles

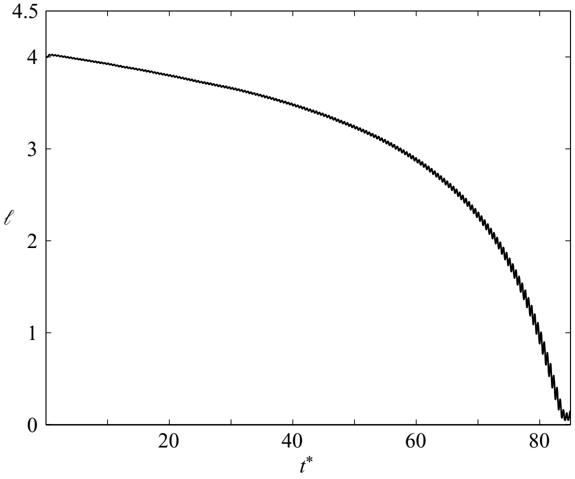

FIGURE 7. Interparticle gap as a function of time for two particles released as shown in figure 6.

are four diameters apart to start with. As noted in the figure, the particles continue to approach each other with time, and eventually become neighbours, corresponding to $\ell \rightarrow 0$. The two particles move in a leader–follower configuration. The rapid decrease in ℓ is due to the acceleration of the follower particle in the wake of the leader. The drafting is shown in a rotating frame in Figure 8. The individual particle trajectories remain helical (similar to the single-particle behaviour, see figure 3), and the centres of the helical trajectories track each other in a clockwise manner (cylinder rotation is counterclockwise) as shown in figure 8. In this configuration, the follower which is in the wake of the leader accelerates towards the leader. This occurs for half of the cylinder rotation, whereas during the other half the leader–follower configuration switches. It must be remembered that this interaction is confined to the mid-transverse plane for this specific case under discussion.

5.1.2. *Kissing of particles*

At the end of drafting, they remain in close proximity to each other in a long-body fashion for a short time duration. When two particles are such that the interparticle gap is less than one particle diameter, the configuration resembles a dumbbell shape. This configuration is referred to as the long-body arrangement. This would correspond to the ‘kissing’ part of motion in the context of rotating flows. This occurs in the vicinity of point A in figure 6.

5.1.3. *Tumbling of particles*

Immediately following the kissing regime (location A in figure 6), the long-body arrangement constituted by the two-particle configuration in very close proximity, is noted to be dynamically unstable. It is well known that a long-body configuration of two particles aligned with the direction of gravity in a Newtonian fluid flow is unstable to small-amplitude disturbances. The instability causes the body to turn such that its broadside is perpendicular to gravity vector (Fortes, Joseph & Lundgren 1987). The cause for the instability is ascribable to small axial perturbations of the long-body axis giving rise to an asymmetric pressure distribution about the rotation axis of the cylinder. It is difficult to quantitatively demonstrate the initiation of such

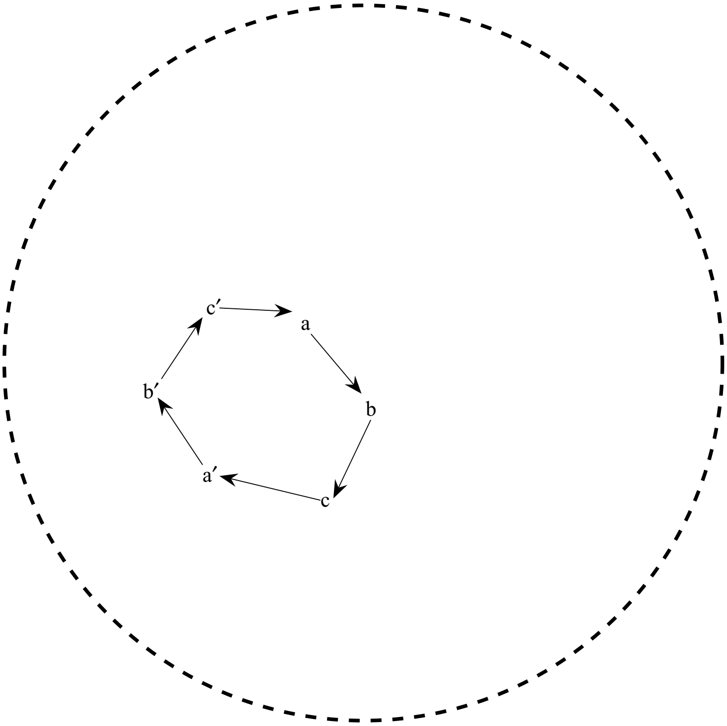

FIGURE 8. Discrete time snapshots of centres of the epitrochoidal trajectories of two-particles as viewed by an observer in a rotating frame (see figure 3). a–b–c and a′–b′–c′ denote the discrete epitrochoidal centres of particles 1 and 2, respectively. This configuration of the leader–follower switches, as is evident from the figure. This process repeats until the interparticle gap is reduced and the particles start tumbling along the axial direction.

an instability, experimentally or numerically. In our numerical computations, the source of the instability may be attributed to the numerical discretization errors and small imperfections in the mesh used for such simulations. However, the phenomenon of axial tumbling is physical. The particles eventually tumble and migrate in opposite directions from the mid-transverse plane (A–B and A–B′, in figure 6) towards the lateral walls, while rotating on transverse planes. This phenomenon of the breakdown of the long-body configuration is referred to as the 'tumbling mechanism'. As seen in figure 9, at A, the particles are aligned such that their line of centres is at right angles to the rotational axis of the cylinder. Owing to the long-body instability, they tumble from position A and start migrating towards the lateral walls. The line of centres during this process changes from $\phi = 90^\circ$ to the lowest value of nearly 10° at about midway during traverse from A to B, B′. We recall that B, B′ are the points of closest approach to the lateral walls.

5.1.4. *Axial migration – 'settling' planes*

Referring to figure 6, subsequent to tumbling, the motion of the particles in the axial direction is dominated by forces exerted both by interparticle and particle–wall interactions. Initially, the separation distance between the particles is small so that particle–particle interaction is dominant. This interaction results in a repulsive force that tends to push the particles away from each other (A–B and A–B′). The particles continue to migrate axially up to locations B and B′ and the repulsive force due to

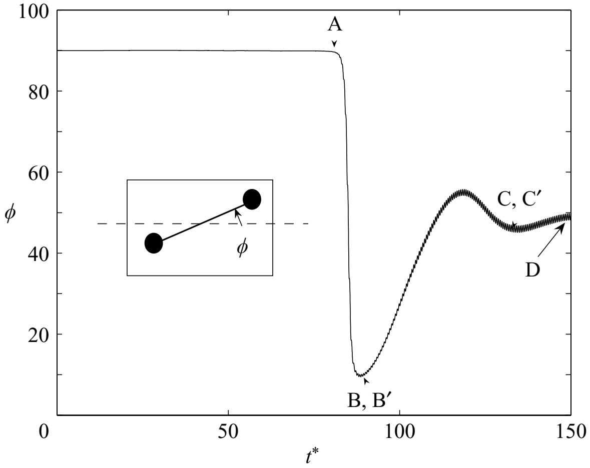

FIGURE 9. The angle ϕ made by the line of centres with the horizontal axis (as shown in the inset schematic). $\phi = 90°$ implies the particles are in the same transverse planes and $\phi = 0$ implies the lines of centres is aligned parallel to the axis of rotation. See figure 6 for the location of the points.

particle–wall interaction has increasing influence, reaching a maximum value at B and B′. Beyond B and B′, the particles move towards each other owing to the dominant particle–wall influence (B–C and B′–C′). During this motion, the competition between the particle–wall and particle–particle interactions become increasingly significant. At C and C′, a near force balance is achieved. Subsequent to this, an eventual force equilibrium is achieved when the particles ‘settle’ on transverse planes denoted by D and D′.

Figure 10 shows the key stages in the interaction dynamics of two particles as observed in an inertial frame of reference. Figure 10(*a*) shows the initial position of particle release, and figures 10(*b*)–10(*d*) show the particle positions at A, B–B′ and D–D′, respectively.

5.2. *Uniqueness of the settling planes*

For two identical particles, for any given Re_p and Re_s, independent of initial conditions at release (locations and planes), the locations of the settling planes (D and D′) are unique and equidistant from the midplane (see, figure 11). This is ascribable to the fact that the settling planes represent planes on which force equilibrium has been attained (particle–particle and particle–wall).

5.3. *Particle motion on settling planes*

When particles are on settling planes (D and D′) (see figure 11), several fascinating particle motions are noted to occur in the transverse direction ((x_i, y_i)-plane) and these will now be discussed in detail. The motions on these planes consist of three different types. The following descriptions depict these motions as viewed by an observer in the laboratory (inertial) frame of reference.

1. Particles in stationary states or fixed equilibrium points.
2. Particles in out-of-phase spiralling motions.
3. Particles in out-of-phase almost-circular orbits (‘pedalling’ motion). This state will hereinafter be referred to as circular orbit.

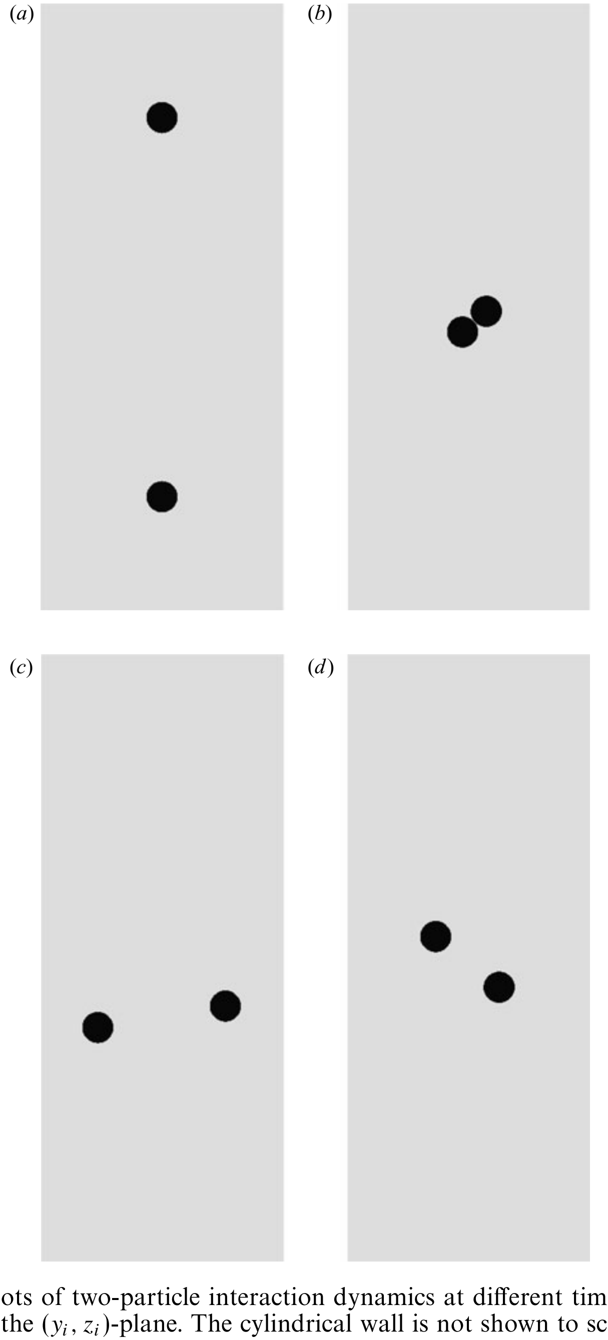

FIGURE 10. Snapshots of two-particle interaction dynamics at different times as viewed by an inertial observer in the (y_i, z_i)-plane. The cylindrical wall is not shown to scale here for clarity. (*a*) Initial position. (*b*) Kissing and tumbling at A. (*c*) Axial migration to B–B′. (*d*) Settling planes D–D′.

For the state of spiralling motion or circular orbit, the particles execute weak axial oscillations about their settling planes, as can be seen in figure 11.

An approximate topology map of the above-mentioned transverse plane states in the $Re_s - Re_p$ space is given in figure 12 for reference.

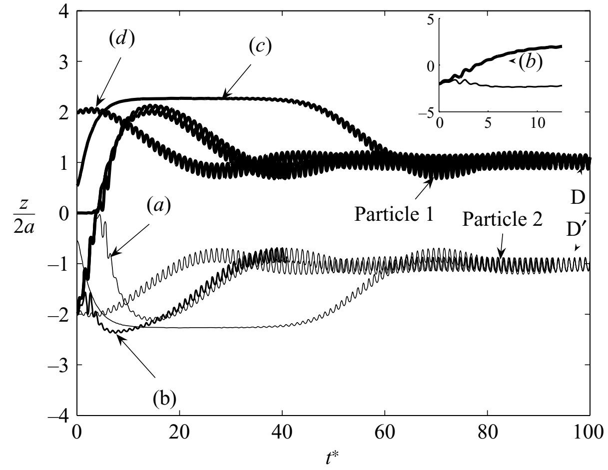

FIGURE 11. Axial positions of the two particles for arbitrarily selected cases in figure 5. Here, (*a*) corresponds to figure 5(*a*), (*b*) corresponds to figure 5(*d*), (*c*) corresponds to figure 5(*f*) with $\delta = 0$, and (*d*) corresponds to figure 5(*h*). Also, the inset shows the enlarged view of (*b*) during the initial transient for clarity.

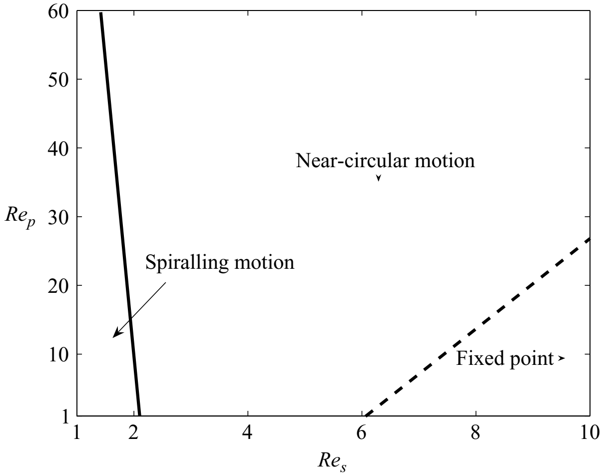

FIGURE 12. An approximate topology map of various stable state configurations (with reference to an inertial frame) as a function of Re_s and Re_p.

5.3.1. *Stationary states*

For low Re_p and high Re_s, for example, $Re_p \sim 5.6$ and $Re_s \sim 8$, the particles after reaching their settling planes, eventually attain stationary or fixed equilibrium points on their corresponding settling planes. These equilibrium points correspond to that which characterizes single-particle equilibrium (see figure 18). However, it may be recalled that fixed equilibrium for a single particle is attained on the mid-transverse plane. The line of centres of the two particles in stationary states is parallel to the rotation axis of the cylinder. The axial and radial positions of the two particles at the stationary state are given in figures 13(*a*) and 13(*b*). The particles settle at fixed points in their respective plane and do not move as viewed by an inertial observer. The particles are not only in force equilibrium with regard to particle–particle and

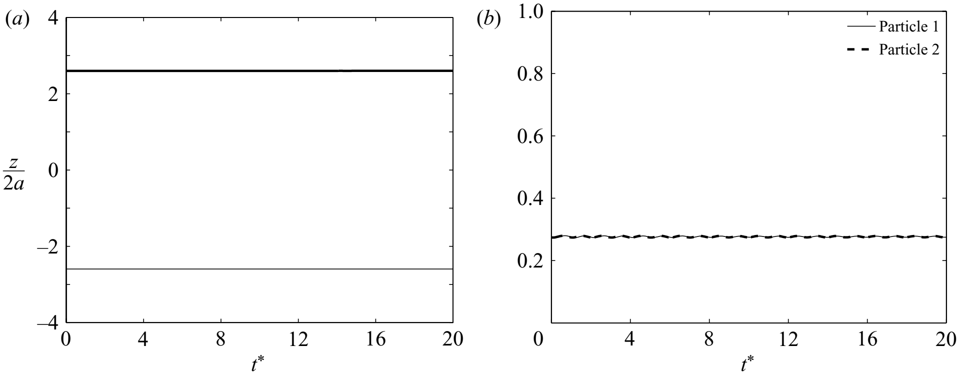

FIGURE 13. Numerical solutions of (*b*) radial position and (*a*) axial migration of two particles at stationary states for $\rho_p/\rho_f = 0.98$, $Re_p \sim 5.6$ and $Re_s \sim 8$.

particle–wall interaction forces, but also with regard to centrifugal force, centrifugal buoyancy, gravitational force, gravitational buoyancy, added mass, pressure, drag, lift and history forces. It may be recalled that the latter forces are typical of a single particle in an equilibrium state. With increasing Re_p, Re_s has to be correspondingly higher to attain these equilibrium states. This has been revealed in our numerical calculations.

5.3.2. *Particles in out-of-phase spiralling motions*

After reaching the settling transverse planes, for all values of Re_p and low values of Re_s, for example $Re_p \sim 5.6$, $Re_s \sim 1$, the particles do not attain equilibrium states on their settling planes; instead, they each execute an out-of-phase spiralling motion (figure 14) about a point on their respective planes (see figure 18). The location of the point about which this motion is executed on each plane corresponds to that which characterizes single-particle equilibrium on the mid-transverse plane. The remarkable feature of these spiralling motions is that, when one particle undergoes an inward spiralling, the other executes an outward spiralling motion (figures 14 and 15). Thus, the spiralling motion is a 'pedalling' motion with the length of the pedal varying with time, the variation being out-of-phase for the two particles. The composite dynamic may therefore be thought of as spiralling motion with the length of the spiral chord increasing on one settling plane while decreasing on the other (out-of-phase manner).

5.4. *Particles in out-of-phase almost-circular orbits: 'pedalling' motion*

For low Re_p and moderate Re_s, and for high Re_p and moderate to high Re_s investigated, for example, consider $Re_p \sim 60$, $Re_s \sim 6$, the particles ultimately move on their respective settling planes in near-circular orbits (figure 16) about fixed points in the planes (see figure 18). The location of the point about which this motion is executed on each plane corresponds to that which characterizes single-particle equilibrium on the mid-transverse plane. Again, the circular motions are out-of-phase. Thus, these circular motions are similar to the spiralling motions, except that the lengths of the spiral chords remain constant and equal (radius of orbit). The small departures from perfect circular orbits as noted in figures 16(*b*) and 16(*c*) are ascribable to the small axial oscillations of the particles about their settling planes.

The projected trajectory on the transverse plane of one particle as noted by an observer attached to the particle on the other plane is circular (figure 17). The perfect out-of-phase motion of the two particles results in the relative trajectory to be circular.

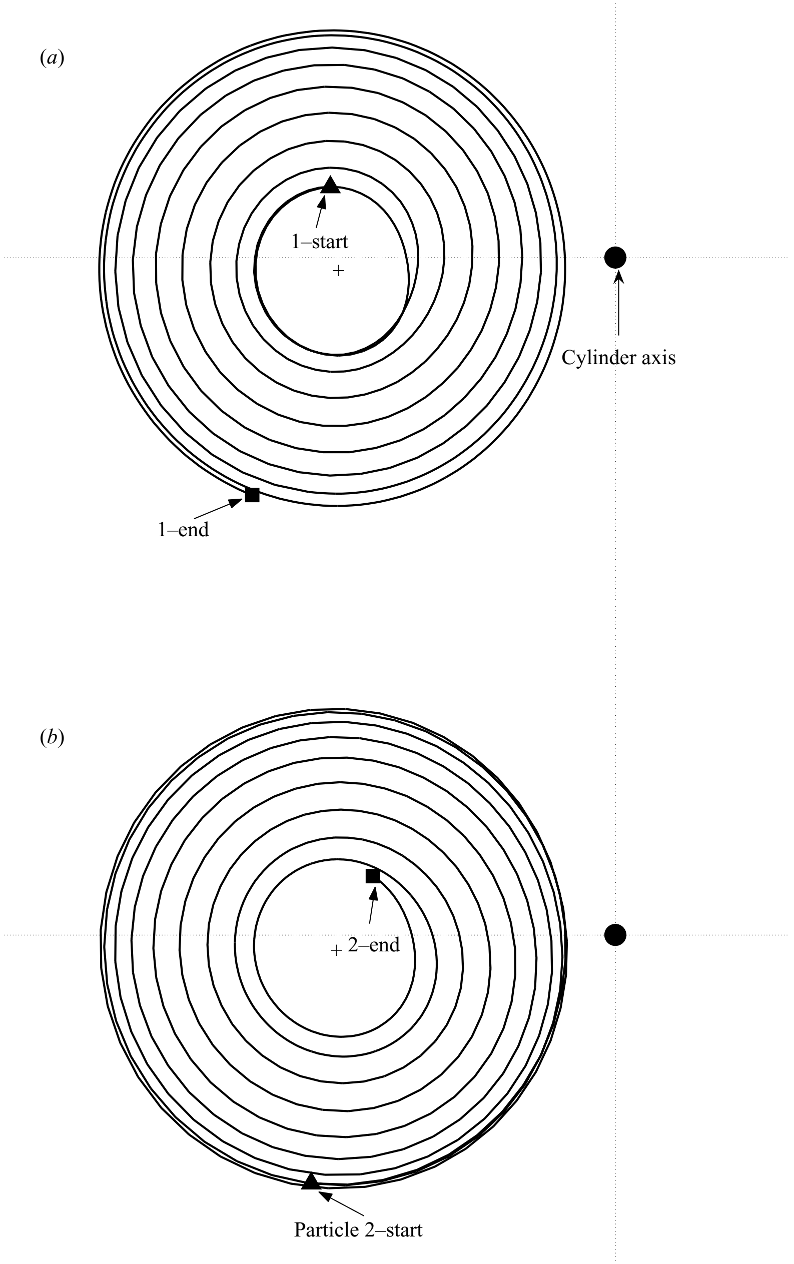

FIGURE 14. The trajectory as observed by an observer in an inertial frame on the transverse (x_i, y_i)-plane for $Re_p \sim 5.6$ and $Re_s \sim 1$ is shown for half the pedalling cycle (the period for which particle 1 spirals out while particle 2 spirals in).

5.5. *Parametric study*

The above studies are extended to include various rotation rates ($1 \leqslant Re_s \leqslant 8$), and Re_p values of 5.6, 14.0, 28.0 and 56, corresponding to the values of $\rho_p/\rho_f = 0.98, 0.95, 0.9$ and 0.8. These are representative of particle parameters in bioreactor studies. As

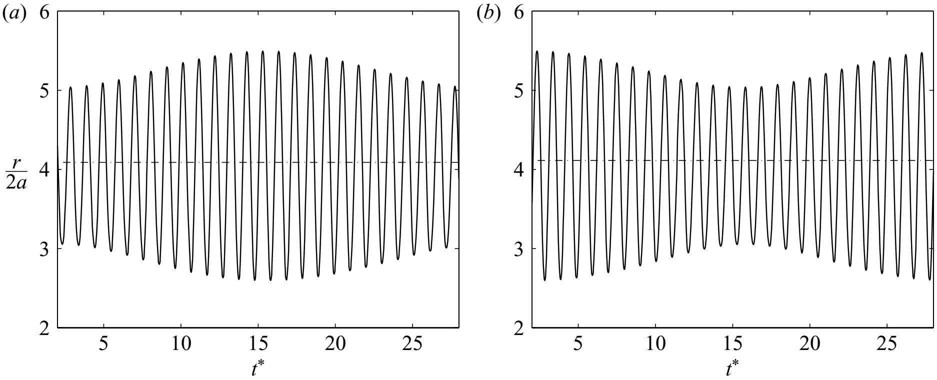

FIGURE 15. Radial positions of the particles as measured from the centre of their corresponding settling planes during the out-of-phase spiralling state. Here, $Re_p \sim 5.6$ and $Re_s \sim 1$. Dotted lines indicate the fixed points on each settling plane about which the spiral orbital motions of the particles take place. (*a*) Particle 1; (*b*) particle 2.

described earlier, the particles may draft, kiss, tumble and migrate or just directly migrate to the eventual settling planes depending on conditions at release.

Upon reaching the settling planes, the particles are noted either to settle at fixed points or to experience spiral or nearly circular orbital motions about such fixed points. As noted from figure 18, it turns out that the coordinates of such fixed points on the transverse planes ((x_i, y_i)-position) coincide with those for single-particle dynamics under identical conditions (recall, however, that single-particle equilibrium points are always located on the mid-transverse plane at $z = 0$). This is a novel feature revealed by this numerical study. For completeness, in figure 18, we display the distances of such equilibrium points from the centre of the settling plane ((x_i, y_i)-plane) for either of the two particles and compare those with the results for single-particle dynamics for various Re_p and Re_s. The comparisons are in absolute accord.

Once the particles come to the settling planes, the forces that come into play are essentially similar to those governing single-particle dynamics on the mid-axial plane. However, they are not identical except for the case where the two particles settle at fixed points on their respective planes. In that particular case, the line of centres of the particles is parallel to the rotation axis of the cylinder. This is seen in figure 19 where we plot the angle ϕ made by the line of centres of the two particles with the rotation axis of the cylinder for various values of Re_p and Re_s after the particles have attained their final state on their settling planes. For $Re_p = 5.6$ and $Re_s = 8$, it is clear that the particles have attained fixed-point equilibrium states ($\phi = 0$) where a perfect symmetry exists about the mid-transverse plane. Depending upon the values of Re_p and Re_s, the line of centres of the two particles may not be horizontal ($\phi \neq 0$). This feature may be explained by examining the states in the immediate neighbourhood of $Re_s = 8$ and $Re_p = 5.6$. By examining the effects in the immediate neighbourhood we are minimizing the role of the change of settling planes themselves. At a fixed Re_s, an increase in Re_p results in $\phi > 0$. Similarly, for a fixed Re_p, a decrease in Re_s results in $\phi > 0$. Changes in Re_p are directly related to changes in density difference and hence to buoyancy forces, whereas changes in Re_s are directly related to rotation rate and hence to centrifugal and Coriolis forces. Thus, non-zero ϕ values are largely ascribable to the combined roles of buoyancy, Coriolis and centrifugal forces on the

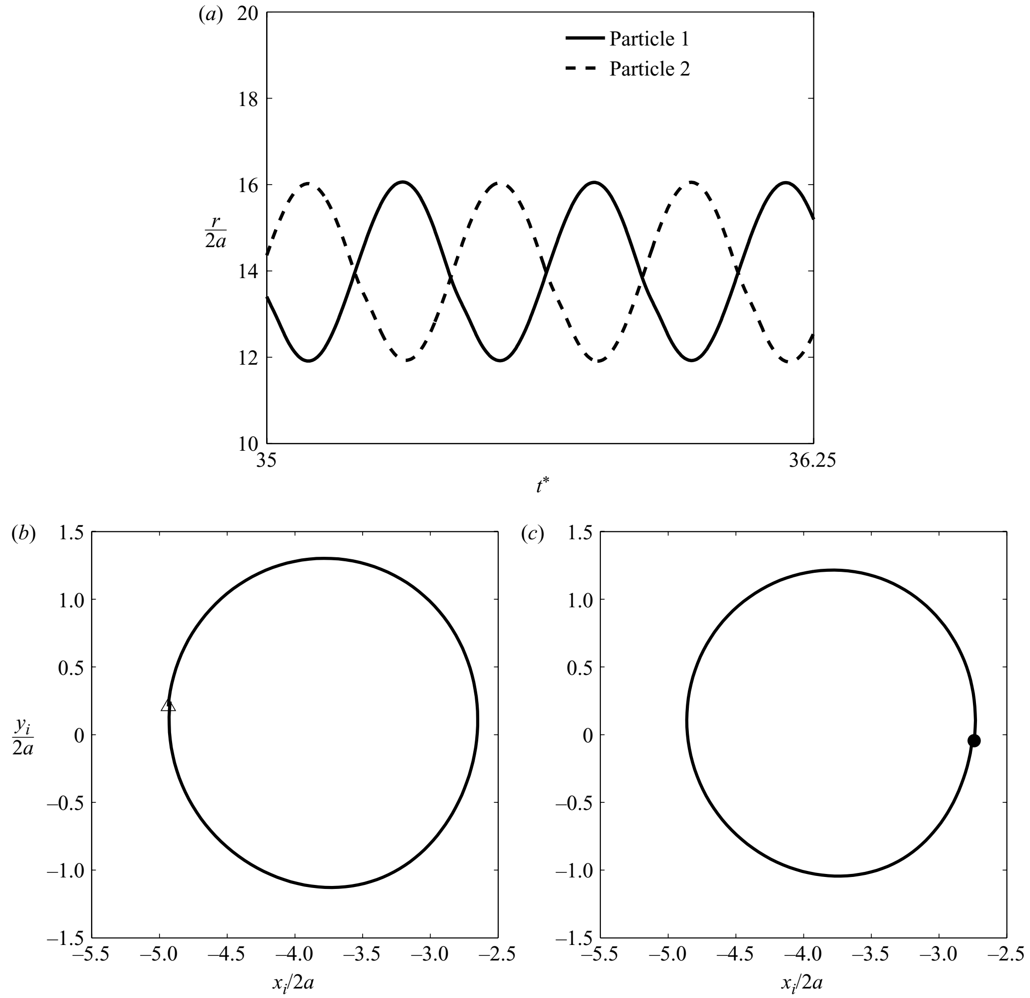

FIGURE 16. (*a*) Radial positions and (*b, c*) trajectories of particles as seen by an inertial observer corresponding to the case of $\rho_p/\rho_f = 0.8$, $Re_p \sim 60$ and $Re_s \sim 6$. The positions of particles 1(●) and 2(△) observed at the same instant showing the out-of-phase behaviour. The particles are seen to undergo near-circular bicycle pedalling motion.

settling planes. Furthermore, a non-zero value of ϕ gives rise to a net outward radial lift to the particles in their respective settling planes causing orbital motions as shown in the Appendix. In figure 19, for the range $5.5 < Re_s < 6.5$ and for $Re_p = 28$, there is characteristically a large increase in ϕ followed by a decrease. In this case, the locations of the settling planes have moved closer to the mid-axial plane resulting in ϕ changing from ~32° to ~42°. We note that the locations of the settling planes are very much controlled by the particle–wall and particle–particle repulsive interactions which in turn depend in a complicated manner on Re_p and Re_s. This will be discussed subsequently with reference to figure 20.

The axial locations of the settling planes for the particles are shown in figure 20. These locations are perfectly symmetric about the mid-axial plane ($z/2a = 0$), and hence only one representative settling plane position is displayed. We note that $z/2a = 4$ indicates the location of a lateral wall. In general, for a given Re_p and

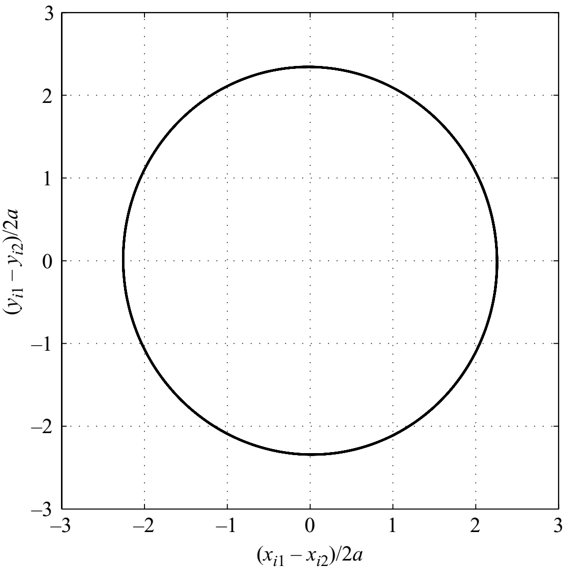

FIGURE 17. Projected trajectory on the transverse plane of one particle as noted by an observer attached to the particle on the other plane.

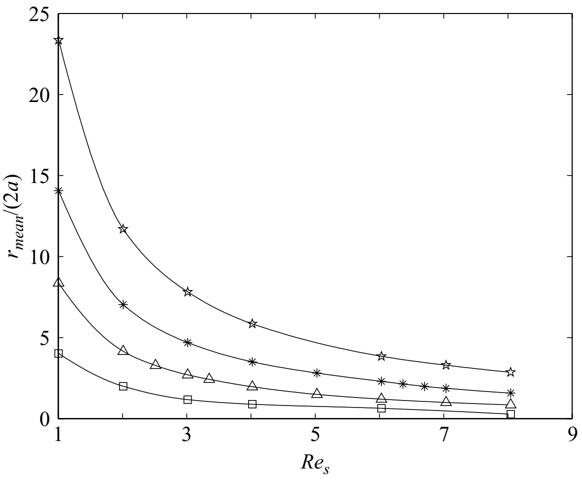

FIGURE 18. The distances of fixed points on the settling plane for each particle as a function of Re_p and Re_s. □, $\rho_p/\rho_f = 0.98$, $Re_p = 5.6$; △, $\rho_p/\rho_f = 0.95$, $Re_p = 14.0$; ∗, $\rho_p/\rho_f = 0.9$, $Re_p = 28.0$; ⋆, $\rho_p/\rho_f = 0.8$, $Re_p = 56$; and solid lines denote single-particle dynamics result (see Appendix). Note the coincidence with fixed equilibrium points for single-particle dynamics at the same Re_p and Re_s.

increasing values of Re_s, the settling plane distances as measured from the mid-axial plane increase. As discussed earlier, under these circumstances, ϕ decreases, increasingly causing the line of centres of the particles to be parallel to the horizontal axis of rotation. As a consequence, the interactive particle–particle repulsive force strength increases, with the result that the distance between the settling planes increases. The final locations of the settling planes, however, are determined by a balance between the particle–particle and particle–wall repulsive forces. For the case

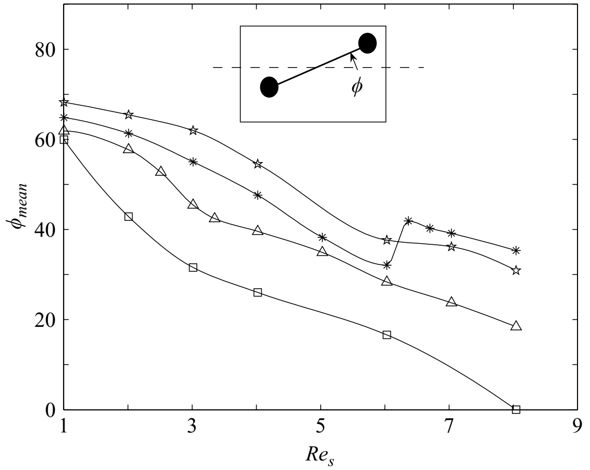

FIGURE 19. The angle ϕ made by the line of centres of the two particles with the rotation (horizontal) axis (see inset) as a function Re_s. □, $\rho_p/\rho_f = 0.98$, $Re_p = 5.6$; △, $\rho_p/\rho_f = 0.95$, $Re_p = 14.0$; ∗, $\rho_p/\rho_f = 0.9$, $Re_p = 28.0$; ⋆, $\rho_p/\rho_f = 0.8$, $Re_p = 56$.

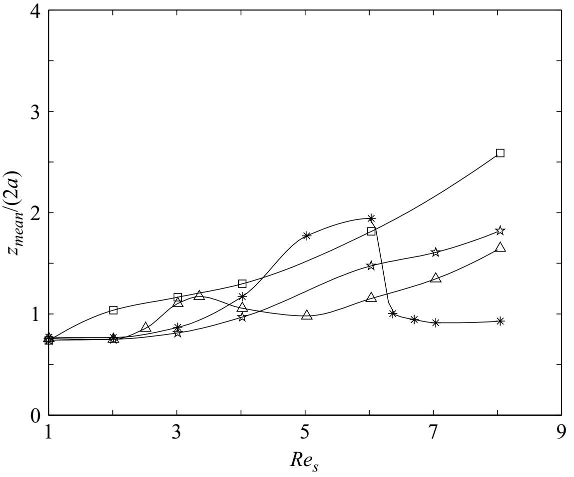

FIGURE 20. The axial positions of the settling planes of the particles as a function of Re_s. □, $\rho_p/\rho_f = 0.98$, $Re_p = 5.6$; △, $\rho_p/\rho_f = 0.95$, $Re_p = 14.0$; ∗, $\rho_p/\rho_f = 0.9$, $Re_p = 28.0$; ⋆, $\rho_p/\rho_f = 0.8$, $Re_p = 56$.

of $Re_p = 28$ and $5.5 < Re_s < 6.5$, a limiting condition is reached where the particle–wall repulsion overwhelms the weakened particle–particle interaction (owing to an increased ϕ) in this narrow range, and the settling planes end up moving closer to each other. Beyond this limiting condition, ϕ decreases and the general trend referred to in the earlier discussion is recovered. A definitive explanation of this feature would require further study.

In figures 21 and 22, the amplitudes of oscillation about the mean radial position and of spiralling motion of each individual particle on their settling planes are shown as a function of Re_s for various Re_p. In figure 21, a value of zero amplitude indicates a state of fixed equilibrium point, while in figure 22 this would correspond to the state

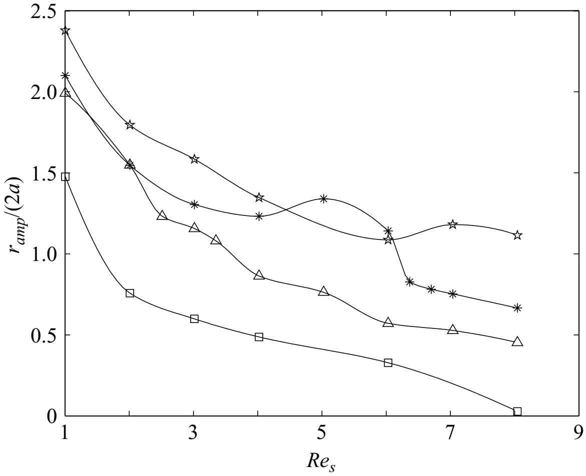

FIGURE 21. The amplitude of oscillation about the mean radial position of each individual particle as a function of Re_s. A value of zero implies an equilibrium fixed-point state. □, $\rho_p/\rho_f = 0.98$, $Re_p = 5.6$; △, $\rho_p/\rho_f = 0.95$, $Re_p = 14.0$; ∗, $\rho_p/\rho_f = 0.9$, $Re_p = 28.0$; ⋆, $\rho_p/\rho_f = 0.8$, $Re_p = 56$.

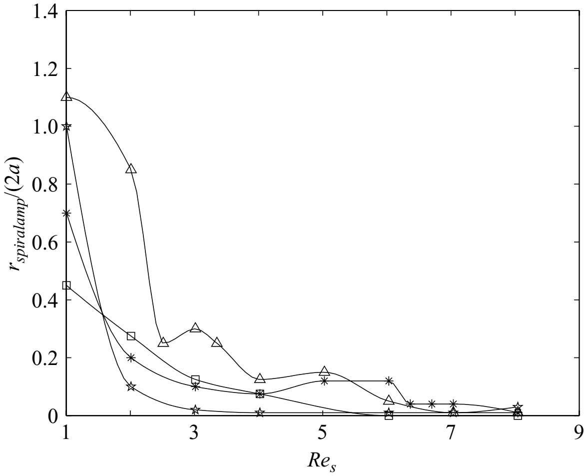

FIGURE 22. The amplitude of spiralling motion of each individual particle as a function of Re_s. A value of zero indicates a perfect circular pedaling motion. □, $\rho_p/\rho_f = 0.98$, $Re_p = 5.6$; △, $\rho_p/\rho_f = 0.95$, $Re_p = 14.0$; ∗, $\rho_p/\rho_f = 0.9$, $Re_p = 28.0$; ⋆, $\rho_p/\rho_f = 0.8$, $Re_p = 56$.

of circular pedalling motion. Generally, for a given Re_p, with increasing Re_s, both the oscillation about the mean radial position and the spiralling amplitude decrease. This is a consequence of a reduction in the radial lift force experienced by each particle. The radial lift forces that arise with two particles on their settling planes are directly related to the particle–particle repulsion (see Appendix for details). At very high values of Re_s, fixed equilibrium points are the stable states. Thus, increasing Re_s (the speed of rotation), has a stabilizing influence.

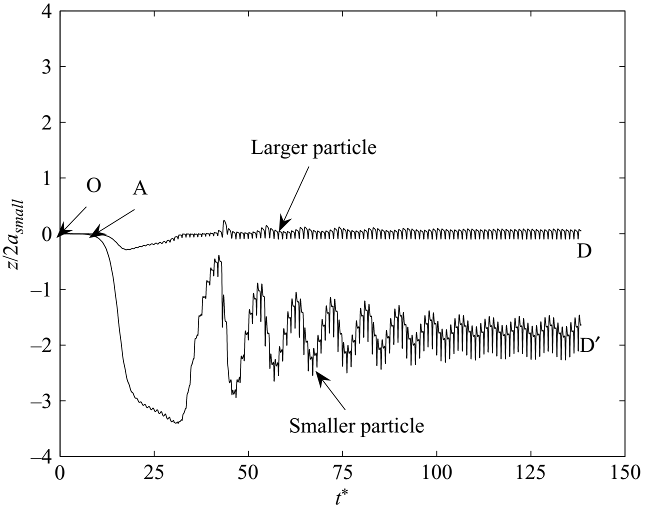

FIGURE 23. Different diameter and same density particles were released close to each other. In the above figures a_{small} refers to the radius of the small particle. Here, a_{small} denotes the radius of the smaller particle.

6. Spherical particles with different densities and diameters

We now examine the cases of two spherical particles with similar densities but different sizes, and two particles of the same size but different densities. By comparison of the results with those for identical particles we are able to investigate the roles of densities and sizes of particle pairs in rotating fluid motion.

6.1. *Case 1. Two particles with same densities but different diameters*

Two particles with the same densities but different sizes are released very close to each other, as given in figure 5(*a*) in a cylinder rotating at a constant rate. The larger particle is twice the size of the smaller and the value of $\rho_p/\rho_f = 0.99$. The Re_p and Re_s for the smaller particle are set to be 2.8 and 1, respectively, while for the larger particle, the corresponding Re_p and Re_s values are $\sim$22.4 and 4, respectively.

Figure 23 shows the time history of the axial positions of the two particles. The two particles are released on the mid-axial plane ($z = 0$), close to each other. They draft, kiss and tumble in axial directions (denoted by O–A). The smaller particle experiences a very large particle–particle repulsive force. This causes it to move away rapidly towards the lateral wall. However, the opposing particle–wall repulsion pushes the smaller particle back towards the mid-axial plane. Over a period of time, this motion is damped and the smaller particle essentially attains a settling plane. On the other hand, the larger particle is very slightly perturbed from its initial axial location and essentially remains on the mid-axial plane. As always, the particles on the settling planes experience small axial oscillations. In this case, owing to the large difference in the sizes of the particles, the smaller one oscillates significantly more, by as much as its diameter. Thus, the settling planes are no longer symmetrically situated with reference to the mid-axial plane, bringing into prominence the roles of particle–particle and particle–wall interactions.

After the attainment of particle–particle and particle–wall force equilibrium, the particles are located on the settling planes (denoted D–D′), and figure 24 displays the characteristics of their subsequent behaviour as a function of time. The smaller

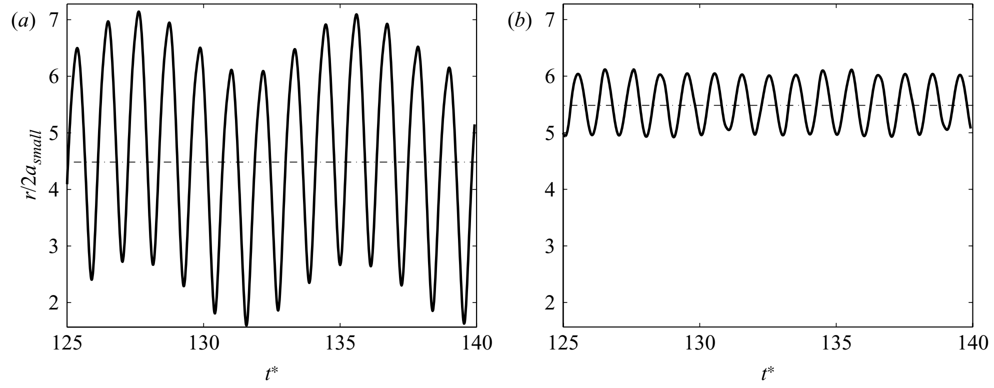

FIGURE 24. Radial positions of the particles as measured from the centres of their corresponding settling planes ($x_i = y_i = 0$) after the attainment of equilibrium states. (*a*) Smaller particle; (*b*) larger particle. Dotted lines indicate the fixed radial points on each settling plane about which the orbital motions of the particles take place. Here, a_{small} denotes the radius of the smaller particle.

particle executes a spiralling motion about its own fixed point while the larger particle is in near-circular orbital motion. These motions, however, do not correspond to pedalling. As would be expected, $\phi \neq 0$. The amplitudes of the orbital motions are significantly different, with the spiralling motion amplitude of the smaller particle being ∼5 times larger than that of the other particle. For the particle sizes considered, the larger particle is most dominant in determining final equilibrium states. The fixed points for the two states are $(x_{i1}, y_{i1}) = (-2.0, -0.1)$ for the smaller particle and $(x_{i2}, y_{i2}) = (-5.5, 0.1)$ for the larger, as observed in an inertial frame of reference.

6.2. *Case 2. Particles with same size diameters but different densities*

Here, two particles of the same size but of different densities (higher to lower density ratio = $\rho_1/\rho_2 \approx 1.24$) are released on the mid-axial plane ($z = 0$) of the rotating cylinder. The Re_p and Re_s corresponding to the higher-density particle ($\rho_p/\rho_f = 0.99$) are ∼2.8 and 1, and that for the lesser density ($\rho_p/\rho_f = 0.8$) are ∼56 and 1, respectively. Note that both the particles are lighter than the fluid in which they are released. Hence, the lighter of the two particles has a higher slip velocity and hence higher Re_p than the other. In other words, the heavier particle is closer to neutral buoyancy than is the lighter one. The non-dimensional particle locations at release are close to each other ($(x, y)_{t=0} = (-25, -0.7)$) for the lighter, and ($(x, y)_{t=0} = (-25, 0.65)$) for the heavier. The particle draft at O–A, kiss and tumble (figure 25). At A, the heavier particle migrates away in the axial direction towards the lateral wall while the lighter one stays on the mid-axial plane. Thus, for the lighter particle, the mid-axial plane is the settling plane. On the mid-axial plane, the lighter particle executes a spiral trajectory as a function of time approaching a fixed-point equilibrium location and this is evident from figure 26(*b*). Note the damping of the amplitude with time. On the other hand, the heavier particle continues to migrate axially, experiencing particle–particle and particle–wall repulsive forces. However, as can be seen from the dotted lines in figure 26(*a*), the particle also drifts away in the radial direction. Hence, the two particles become farther apart with time. Beyond a certain time indicated by B′ (see figure 25), the particle–particle interaction is so weak that the particle–wall forces exceed the former. Hence, the particle starts migrating towards the mid-axial plane.

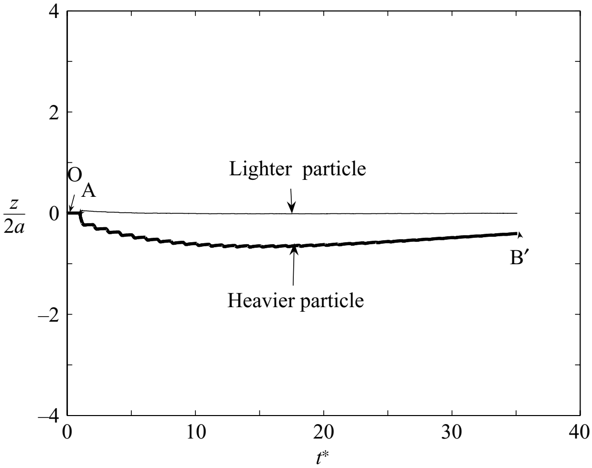

Figure 25. Axial migration of two particles with different densities but the same size released close to each other. The heavier of the two is released far away from its equilibrium point.

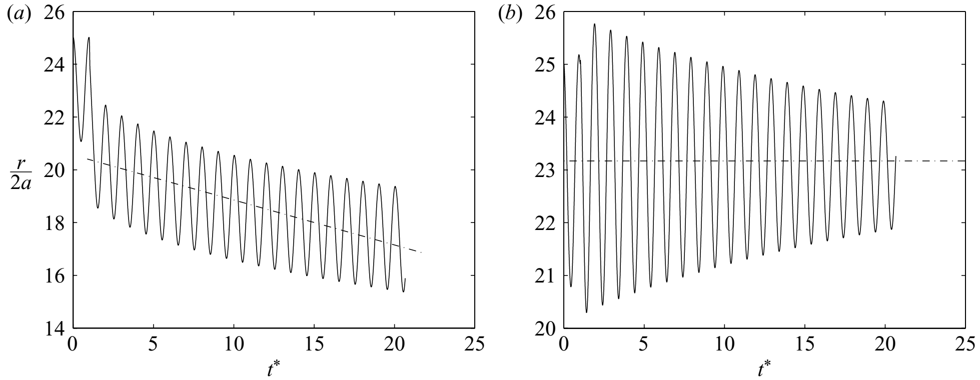

Figure 26. Normalized radial position histories of the particles released close to each other. (*a*) Heavier of the two particles. (*b*) Lighter of the two particles.

The heavier particle eventually migrates towards the mid-axial plane, at a location far from the equilibrium point of the lighter particle.

To confirm this speculation, we have carried out another study with the same particles, where we have chosen the release locations to coincide with the fixed equilibrium points that each of the individual particles would have attained had they been released individually on the mid-axial plane. We calculated these locations by solving the single-particle dynamics formulation (see (27) with lift and history forces set to zero). These happen to be far apart with the lighter-particle equilibrium location being $((x_i, y_i) = (-23.1, 0.9))$ and the heavier $((x_i, y_i) = (-2.0, -0.1))$. For these conditions, the two particles do not migrate in the transverse direction, as seen in figure 27, owing to the wide separation of equilibrium points. The lighter of the two particles has a larger wake intensity because of a higher slip velocity. It significantly affects only the radial motion of the relatively heavier particle whose wake intensity is smaller owing to smaller slip velocity. Thus, while the lighter particle approaches

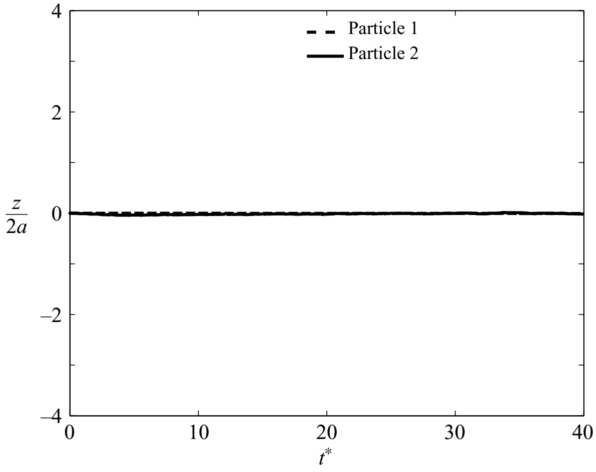

FIGURE 27. Axial migration of two particles with different densities but the same size released closer to their respective equilibrium points that are far away from each other.

the fixed point, the heavier one is greatly perturbed by the other particle's wake and goes into a circular motion about a mean radial position (see figure 28). Note that the amplitude of circular motion as noted from figure 28(*b*) does not decay for the heavier of the two particles. This case demonstrates two-dimensional wake interaction effects owing to the wide separation of the mean radial positions of the particles.

7. Conclusion

The main conclusions of the present study are as follows.

1. For all cases of particle and shear Reynolds numbers investigated, two identical spherical lighter-than-fluid particles, independent of the location of their release, eventually axially migrate towards and settle on transverse planes that are symmetric about the mid-transverse plane of the cylinder. Upon settling, the particles may attain three distinctly different possible states, as noted by an observer in an inertial frame of reference. These states are: (i) fixed equilibrium points; (ii) out-of-phase spiralling motion about such equilibrium points on their settling planes; and (iii) out-of-phase circular orbital motion about such equilibrium points on their settling planes. The out-of-phase circular orbital motion resembles bicycle pedalling.

2. The three states describes in item 1 are due to particle–particle and particle–wall interaction force equilibrium.

3. The behaviours of two non-identical particles (same density but different sizes, or same size but different densities) are different from those of identical particles. For example, non-identical particles may both end up settling on the mid-transverse plane. This occurs when the locations of their corresponding single-particle equilibrium points are far apart. When such points are not far apart, particles may settle on planes that may not be symmetrical about the mid-transverse plane. While located on their settling planes, their equilibrium states may not be similar. For example, for particles of the same density but of different sizes, the smaller of the two may execute a spiralling motion whereas the larger is in near-circular orbital motion. With particles of the same size but of different densities, while the lighter of the two approaches

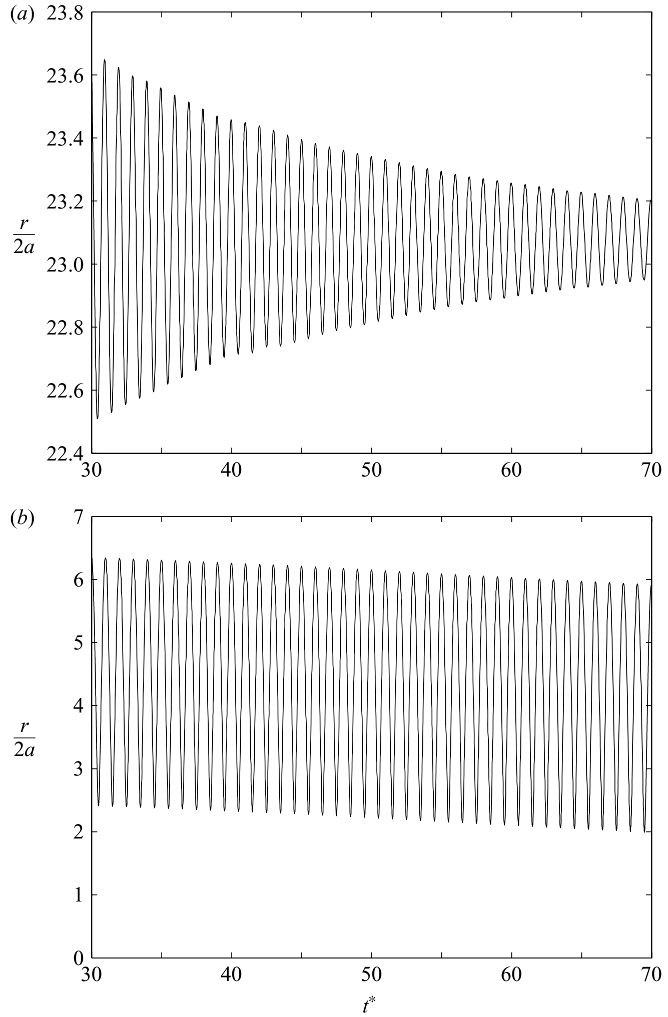

FIGURE 28. Normalized radial position histories of the particles released far away but closer to their respective equilibrium points. (*a*) Normalized radial position of the lighter of the two particles. (*b*) Normalized radial position of the heavier of the two particles.

its equilibrium point on the mid-axial plane, the heavier one experiences a circular motion on the same plane about its equilibrium point.

4. The roles of particle–particle and particle and particle–wall interactions are dominant in deciding the final states of the particles.

5. In order to numerically simulate two-particle motion at various ρ_p/ρ_f, Re_p and Re_s in a fluid-filled cylinder rotating about a horizontal axis, the rotating frame is preferred for computational purposes.

The authors would like to gratefully acknowledge NASA Grant NAG 9-1400 for supporting this work. H. H. H. would also like to acknowledge the partial support by the Nano/Bio interface center through NSF NSEC DMR-045780.

Appendix

A.1. *A simplified analysis for the state of near-circular motion of each particle in its settling plane*

We now present a simplified analysis for describing the dynamical stability of the two-particle system which corresponds to the particles undergoing near-circular motion about equilibrium points on their respective planes. The system will be analysed in the vicinity of the equilibrium point that is characteristic of single-particle dynamics. At the equilibrium point, the major forces acting on the particle, such as the gravitational weight and buoyancy, centrifugal force and centrifugal buoyancy, drag, lift and other history forces are almost in balance with each other.

Consider equation (27) in $x_i - y_i$ inertial Cartesian coordinates with $\boldsymbol{F}_L$ set equal to 0. For simplicity, the subscript i will be dropped. Here, the absence of the subscript i does not imply the use of rotating frame coordinates.

$$\rho_p V_p \frac{\mathrm{d}\boldsymbol{U}_p}{\mathrm{d}t} + C_v \rho_f V_p \left(\frac{\mathrm{d}\boldsymbol{U}_p}{\mathrm{d}t} - \frac{\mathrm{D}\boldsymbol{U}_f}{\mathrm{D}t} \right) = -V_p \nabla p + (\rho_p - \rho_f) V_p g + \boldsymbol{F}_D. \tag{A 1}$$

With $\boldsymbol{U}_f = -\omega y \hat{\boldsymbol{i}} + \omega x \hat{\boldsymbol{j}}$, where $\hat{\boldsymbol{i}}$, $\hat{\boldsymbol{j}}$ are the unit vectors along the x and y directions, and $\mathrm{D}\boldsymbol{U}_f/\mathrm{D}t = -\omega^2 x \hat{\boldsymbol{i}} - \omega^2 y \hat{\boldsymbol{j}}$, (A 1) may be written in component form as follows:

$$V_p \left(\rho_p + \tfrac{1}{2}\rho_f \right) \frac{\mathrm{d}u}{\mathrm{d}t} = -\tfrac{3}{2} V_p \rho_f \omega^2 x - C_D (u + \omega y), \tag{A 2}$$

$$V_p \left(\rho_p + \tfrac{1}{2}\rho_f \right) \frac{\mathrm{d}v}{\mathrm{d}t} = -\tfrac{3}{2} V_p \rho_f \omega^2 y - C_D (v - \omega x) + V_p (\rho_f - \rho_p) g. \tag{A 3}$$

In (A 2) and (A 3), u, v denote the x, y velocity components of the particle, and C_D is the drag coefficient. With $C_D = 6\pi \mu_f a$, (A 2) and (A 3) can be written as the following coupled first-order equations:

$$\frac{\mathrm{d}x}{\mathrm{d}t} = u, \tag{A 4a}$$

$$\frac{\mathrm{d}y}{\mathrm{d}t} = v, \tag{A 4b}$$

$$\frac{\mathrm{d}u}{\mathrm{d}t} = -\frac{3\alpha(\omega)^2 x}{2} - \frac{u + \omega y}{\tau}, \tag{A 4c}$$

$$\frac{\mathrm{d}v}{\mathrm{d}t} = -\frac{3\alpha(\omega)^2 y}{2} - \frac{v - \omega x}{\tau} + \frac{\rho_f - \rho_p}{\rho_f/2 + \rho_p} g. \tag{A 4d}$$

In (A 4), $\alpha = \rho_f/(\rho_f/2 + \rho_p)$ and $\tau = 2a^2(\rho_f/2 + \rho_p)/9\mu_f$. The linear system represented by (A 4) can be compactly written as:

$$\frac{\mathrm{d}}{\mathrm{d}t} \begin{pmatrix} x \\ y \\ u \\ v \end{pmatrix} = \boldsymbol{A} \begin{pmatrix} x \\ y \\ u \\ v \end{pmatrix} + \begin{pmatrix} 0 \\ 0 \\ 0 \\ \dfrac{\rho_f - \rho_p}{\rho_f/2 + \rho_p} g \end{pmatrix}, \tag{A 5}$$

where

$$\boldsymbol{A}=\begin{pmatrix} 0 & 0 & 1 & 0 \\ 0 & 0 & 0 & 1 \\ -3\alpha\omega^2/2 & -\omega/\tau & -1/\tau & 0 \\ \omega/\tau & -3\alpha\omega^2/2 & 0 & -1/\tau \end{pmatrix}. \tag{A 6}$$

The eigenvalues of $\boldsymbol{A}$ will determine the stability of the system. The characteristic equation for the eigenvalues is given by

$$\det(\boldsymbol{A}-\lambda \boldsymbol{I})=0. \tag{A 7}$$

By letting $\epsilon=\omega\tau$ and $\bar{\lambda}=\lambda/\omega$, (A 7) can be shown to be

$$\bar{\lambda}^2(1+\epsilon\bar{\lambda})^2+3\alpha(\epsilon\bar{\lambda})^2+3\alpha\epsilon\bar{\lambda}+9\alpha^2\epsilon^2/4+1=0. \tag{A 8}$$

Here, ϵ may be interpreted as the ratio of the particle time scale, τ, to that of the vortex time scale, $1/\omega$ (Ferry & Balachandar 2001). With the velocity scale used in the present study, namely, $U_{slip}=(2|\Delta\rho|a^2g/9\mu_f)$, it can be shown that $\epsilon\approx 0.06Re_s((\rho_p/\rho_f)+0.5)$. In our analysis, $\rho_p/\rho_f \sim O(1)$ and for $Re_s \sim O(1)$ (moderate rotation rates), $\epsilon \ll 1$. For such small values of ϵ, we seek solutions of the form $\bar{\lambda}=\mathrm{i}+\epsilon\eta_1+\epsilon^2\eta_2+O(\epsilon^3)$, where η_1, η_2 are, in general, complex numbers. Solutions for η_1, η_2 may then be obtained by using (A 8), and by equating like powers in ϵ. After simplification, we obtain

$$\lambda=-\omega^2\tau\Delta\bar{\rho}+\mathrm{i}\omega[1+2(\omega\tau)^2\Delta\bar{\rho}(\rho_p-\rho_f/2)/\rho_f/2+\rho_p], \tag{A 9}$$

where, $\Delta\bar{\rho}=(\rho_f-\rho_p)/(\rho_f/2+\rho_p)$. For $\rho_p<\rho_f$, the real part of (A 9) is negative, and therefore the system is stable.

A.2. *Equilibrium point on the settling plane*

The stable equilibrium-state solution can be obtained from (A 2) and (A 3), by setting the first and second derivatives of x, y to be zero. After simplification, this yields the following solution for the radial position, r_{eq} $(=\sqrt{x_{eq}{}^2+y_{eq}{}^2})$, and the angular position, θ_{eq} $(=\tan^{-1}(y_{eq}/x_{eq}))$ (Gao *et al.* 1997):

$$r_{eq}=\frac{(\rho_f-\rho_p)V_pg}{\omega\sqrt{[m_f(C_v+1)\omega]^2+C_D{}^2}}, \tag{A 10}$$

$$\theta_{eq}=\tan^{-1}\left(\frac{m_f(C_v+1)\omega}{-C_D}\right). \tag{A 11}$$

For $C_D=6\pi\mu_f a$, $m_f(C_v+1)\omega/C_D\approx 0.06Re_s(C_v+1)$. With $C_v=0.5$ for a sphere and for $Re_s\sim O(1)$, $C_D \gg m_f(C_v+1)\omega$, and the (A 10) simplifies to:

$$r_{eq}=\frac{(\rho_f-\rho_p)V_pg}{\omega C_D} \tag{A 12}$$

A.3. *Dynamical stability about the equilibrium point on the settling plane*

Next, we consider the dynamical stability of the system represented by (A 5) by perturbation in the vicinity of the equilibrium point given by (A 12) and (A 11). The perturbation is by a small but constant force, $F_{perturb}=m_p\bar{\gamma}$, acting in the outward radial direction about the equilibrium point. This force has components, $[m_p\bar{\gamma}x/r_{eq}, m_p\bar{\gamma}y/r_{eq}]$, along the Cartesian (x, y) directions about the equilibrium point. The dynamical system may now be expressed as follows:

$$\frac{\mathrm{d}x}{\mathrm{d}t} = u, \tag{A 13a}$$

$$\frac{\mathrm{d}y}{\mathrm{d}t} = v, \tag{A 13b}$$

$$\frac{\mathrm{d}u}{\mathrm{d}t} = -\frac{3\alpha(\omega)^2 x}{2} - \frac{u+\omega y}{\tau} + \gamma x, \tag{A 13c}$$

$$\frac{\mathrm{d}v}{\mathrm{d}t} = -\frac{3\alpha(\omega)^2 y}{2} - \frac{v-\omega x}{\tau} + \frac{\rho_f - \rho_p}{\rho_f/2+\rho_p} g + \gamma y, \tag{A 13d}$$

where $\gamma = \bar{\gamma}/r_{eq}$ may be assumed to be a constant in the neighbourhood of r_{eq}. With a dynamic stability analysis similar to the previous one, the following eigenvalues govern stability:

$$\lambda = \tau(-\omega^2 \Delta\bar{\rho} + \gamma) + \mathrm{i}\omega + O(\epsilon^2). \tag{A 14}$$

In (A 14), the real part of λ vanishes for $\gamma = \omega^2 \Delta\bar{\rho}$, thus implying neutral stability in that case. With $\gamma = \omega^2 \Delta\bar{\rho}$, the magnitude of $F_{perturb}$, is given by:

$$F_{perturb} = \Delta\bar{\rho}\omega^2 r_{eq} m_p. \tag{A 15}$$

The net gravitational weight (weight of the particle minus buoyancy) acting on the particle is:

$$F_g = (m_f - m_p)g. \tag{A 16}$$

Therefore, the ratio of the forces becomes:,

$$\frac{F_{perturb}}{F_g} \approx 0.06\ Re_s \left(1 - \frac{\rho_p}{\rho_f}\right) \left(\frac{1}{1+\frac{1}{2}(\rho_p/\rho_f)}\right). \tag{A 17}$$

For $\rho_p/\rho_f \sim O(1)$ and for moderate rotation rates ($Re_s \sim O(1)$), $F_{perturb}/F_g \ll 1$.

For higher Re_p, we may write $C_D = 6\pi\mu_f a\beta$, where, $\beta = \beta(Re_p) \geqslant 1$, is a drag modification factor, which, in general is a function of Re_p. Then,

$$\frac{F_{perturb}}{F_g} \approx \frac{0.06}{\beta}\ Re_s \left(1 - \frac{\rho_p}{\rho_f}\right) \left(\frac{1}{1+\frac{1}{2}(\rho_p/\rho_f)}\right). \tag{A 18}$$

Under appropriate conditions, we note that a force of small magnitude is all that is necessary to make the system neutrally stable. The assumed functional dependence of this radial force (locally linear about the equilibrium point) causes the fixed-point solution to be unstable which may correspond to the solution of limit cycles (circular orbits). In the context of two-particle dynamics, $F_{perturb}$ arises owing to particle–particle repulsive force, as will be demonstrated in the subsequent section.

A.4. *Particle–particle interaction forces*

In § 5.4, we demonstrated that when a particle (of the two-particle system) is eventually located on its settling plane, the particle may execute a circular orbital motion about the equilibrium point (in its own plane) corresponding to single-particle dynamics.

Hence, we will consider two identical particles located on their settling planes and executing circular orbital motions. In particular, we will investigate by a simplified analysis the various forces at play which result in the particles executing out-of-phase motion corresponding to pedalling. Since the axial force balances between particle–particle and particle–wall (z-directional forces) are only required in ascertaining the locations of settling planes, they will not be considered to play any further role in the following development.

At the outset, it may be conjectured that pedalling motions on their respective settling planes must arise as a consequence of particle–particle interaction forces along (x, y)-directions. On this basis, consider the in-plane force balance (x, y-directions) on each particle in an inertial Cartesian frame of reference. With simplification, the equations governing particle motion in its own settling plane may be shown to be governed as follows.

Particle 1

$$\frac{\mathrm{d}u_1}{\mathrm{d}t} = -\frac{3\alpha(\omega)^2 x_1}{2} - \frac{(u_1 + \omega y_1)}{\tau} + \frac{\bar{F}_x}{V_p(\rho_p + \rho_f/2)}, \tag{A 19}$$

$$\frac{\mathrm{d}v_1}{\mathrm{d}t} = -\frac{3\alpha(\omega)^2 y_1}{2} - \frac{(v_1 - \omega x_1)}{\tau} + \frac{\rho_f - \rho_p}{\rho_f/2 + \rho_p} g + \frac{\bar{F}_y}{V_p(\rho_p + \rho_f/2)}. \tag{A 20}$$

Particle 2

$$\frac{\mathrm{d}u_2}{\mathrm{d}t} = -\frac{3\alpha(\omega)^2 x_2}{2} - \frac{(u_2 + \omega y_2)}{\tau} - \frac{\bar{F}_x}{V_p(\rho_p + \rho_f/2)}, \tag{A 21}$$

$$\frac{\mathrm{d}v_2}{\mathrm{d}t} = -\frac{3\alpha(\omega)^2 y_2}{2} - \frac{(v_2 - \omega x_2)}{\tau} + \frac{\rho_f - \rho_p}{\rho_f/2 + \rho_p} g - \frac{\bar{F}_y}{V_p(\rho_p + \rho_f/2)}. \tag{A 22}$$

In contrast to the single-particle dynamics, here, $\bar{F}_x$, $\bar{F}_y$ are the additional forces acting on the (x, y)-settling planes of each particle owing to particle–particle interactions. Let (x_i, y_i) and $\boldsymbol{U}_f = (u_i, v_i)$ denote the instantaneous position and velocity of the particle $i, (i = 1, 2)$, respectively. Also, let $x_r = x_1 - x_2, y_r = y_1 - y_2, u_r = u_1 - u_2, v_r = v_1 - v_2$, denote the relative positions and coordinates, respectively, and let $F_x = \bar{F}_x/V_p(\rho_p + \rho_f/2)$ and $F_y = \bar{F}_y/V_p(\rho_p + \rho_f/2)$ be the forces. The equations governing the relative trajectory may be derived from the above equations by subtraction of one from the other to yield:

$$\frac{\mathrm{d}u_r}{\mathrm{d}t} = -\frac{3\alpha(\omega)^2 x_r}{2} - \frac{(u_r + \omega y_r)}{\tau} + 2F_x, \tag{A 23}$$

$$\frac{\mathrm{d}v_r}{\mathrm{d}t} = -\frac{3\alpha(\omega)^2 y_r}{2} - \frac{(v_r - \omega x_r)}{\tau} + 2F_y. \tag{A 24}$$

If we considered the trajectory of the two particles in their own planes to be circular and out-of-phase, it is possible to describe the nature of the interaction forces which cause such trajectories. Towards this, let $x_r = \psi \cos \omega t$, $y_r = \psi \sin \omega t$ where ψ is the distance between the particles projected on a transverse plane. With, $u_r = \mathrm{d}x_r/\mathrm{d}t$, $v_r = \mathrm{d}y_r/\mathrm{d}t$, we may solve for F_x and F_y from which $\bar{F}_x$ and $\bar{F}_y$ can be produced. This yields,

$$\bar{F}_x = V_p \left(\frac{\rho_f}{2 + \rho_p}\right) \frac{\omega^2}{2} \left(\frac{3\alpha}{2} - 1\right) x_r, \tag{A 25}$$

$$\bar{F}_y = V_p \left(\frac{\rho_f}{2 + \rho_p}\right) \frac{\omega^2}{2} \left(\frac{3\alpha}{2} - 1\right) y_r. \tag{A 26}$$

We may now compare the orders of magnitudes of these interaction forces with the net weight acting on the particle ($F_g = V_p(\rho_f - \rho_p)g$). Assuming $x_r, y_r \sim O(2a)$, it may be shown that,

$$\frac{\bar{F}_{x,y}}{F_g} \approx 0.03 \left(1 - \frac{\rho_p}{\rho_f}\right) \frac{{Re_s}^2}{Re_p}, \tag{A 27}$$

and for $\rho_p/\rho_f \sim O(1)$, $Re_s \sim O(1)$, from (A 27), $\bar{F}_{x,y}/F_g \ll 1$.

A feature of (A 25) and (A 26) is that, with reference to the centre of each particle, these force representations are repulsive in nature (pointing towards the centre of each particle). Particle–particle repulsive forces have also been observed in the studies of interaction of two spherical particles placed side by side whose line of centres is perpendicular to the direction of uniform stream (Kim, Elghobashi & Sirignano 1993; Folkersma, Stein & van der Vosse 2000). The small repulsive force acting on each particle, when projected onto their respective settling planes, would result in a radially outward pointing force (if the line of centres is not aligned parallel to the cylinder axis, i.e. $\phi \neq 0$ in figure 19). This observation corroborates the functional form of the perturbation force assumed in the stability analysis given in the previous section.

REFERENCES

Annamalai, P. & Cole, R. 1986 Particle migration in rotating liquids. *Phys. Fluids* **29** (3), 647–649.

Ayyaswamy, P. S. & Mukundakrishnan, K. 2007 Optimal conditions for simulating microgravity employing NASA designed rotating wall vessels. *Acta Astronaut.* **60**, 397–405.

Bagchi, P. & Balachandar, S. 2002 Shear versus vortex-induced lift force on a rigid sphere at moderate. *Re*. *J. Fluid Mech.* **473**, 379–388.

Coimbra, C. F. M. & Kobayashi, M. H. 2002 On the viscous motion of a small particle in a rotating cylinder. *J. Fluid Mech.* **469**, 257–286.

Ferry, J. P. & Balachandar, S. 2001 A fast Eulerian method for dispersed two-phase flow. *Intl J. Multiphase Flow* **27**, 1199–1226.

Folkersma, R., Stein, H. N. & van der Vosse, F. N. 2000 Hydrodynamic interactions between two identical spheres held fixed side by side against a uniform stream directed perpendicular to the line connecting the spheres' centres. *Intl J. Multiphase Flow* **26**, 877–887.

Fortes, A., Joseph, D. D. & Lundgren, D. D. 1987 Nonlinear mechanics of fluidization of beds of spherical particles. *J. Fluid Mech.* **177**, 483–497.

Gao, H., Ayyaswamy, P. S. & Ducheyne, P. 1997 Dynamics of a microcarrier particle in the simulated microgravity environment of a rotating-wall vessel. *Micrograv. Sci. Technol.* **X** (3), 154–165.

Hu, H. H. 1996 Direct simulation of flows of solid–liquid mixtures. *Intl J. Multiphase Flow* **22**, 335–352.

Hu, H. H., Patankar, N. A. & Zhu, M. Y. 2001 Direct numerical simulations of fluid–solid systems using the arbitrary Lagrangian–Eulerian technique. *J. Comput. Phys.* **169**, 427–462.

Kim, I., Elghobashi, S. & Sirignano, W. A. 1993 Three-dimensional flow over two spheres placed side by side. *J. Fluid Mech.* **246**, 465–488.

Lee, J. & Ladd, A. J. C. 2002 Axial segregation in a cylindrical centrifuge. *Phys. Rev. Lett.* **10**, 1–4.

Lipson, S. G. 2001 Periodic banding in crystallization from rotating supersaturated solutions. *J. Phys.: Condens. Matter* **13**, 5001–5008.

Lynch, S. V., Mukundakrishnan, K., Benoit, M. R., Ayyaswamy, P. S. & Matin, A. 2006 *Escherichia coli* biofilms formed under low shear modeled microgravity in a ground-based system. *Appl. Environ. Microbiol.* **72**, 7701–7710.

Matson, W. R., Ackerson, B. J. & P. Tong, P. 2003 Pattern formation in a rotating suspension of non-Brownian settling particles. *Phys. Rev.* E **67** (050301(R)).

Maxey, R. M. & Riley, J. J. 1982 Equation of motion for a small rigid sphere in a nonuniform flow. *Phys. Fluids* **26** (4), 883–889.

Michaelides, E. E. 2003 Hydrodynamic force and heat/mass transfer from particles, bubbles, and drops. The Freeman Scholar Lecture. *Trans. ASME* I: *J. Fluids Engng* **125**, 209–238.

Minkov, E., Ungarish, M. & Israeli, M. 2000 The motion generated by a rising particle in a rotating fluid – numerical solutions. Part 1. A short container. *J. Fluid Mech.* **413**, 111–148.

Minkov, E., Ungarish, M. & Israeli, M. 2002 The motion generated by a rising particle in a rotating fluid – numerical solutions. Part 2. The long container case. *J. Fluid Mech.* **454**, 345–364.

Mukundakrishnan, K. 2005 Fluid mechanics and mass transfer in rotating wall vessels: a numerical and experimental study. PhD thesis, University of Pennsylvania.

Mullin, T., Li, Y., Del Pino, C. & Ashmore, J. 2005 An experimental study of fixed points and chaos in the motion of spheres in a Stokes flow. *IMA J. Appl. Maths* **70**, 666–676.

Ramirez, L. E. S., Lim, E. A., Coimbra, C. F. M. & Kobayashi, M. H. 2004 On the dynamics of a spherical scaffold in rotating wall bioreactors. *Biotechnol. Bioeng.* **84**, 382–389.

Roberts, G. O., Kornfeld, D. M. & Fowlis, W. W. 1991 Particle orbits in a rotating liquid. *J. Fluid Mech.* **229**, 555–567.

Schiller, L. & Nauman, A. 1933 Uber die grundlegende berechnung bei der schwekraftaubereitung. *Ver. Deutch. Ing.* **44** (11), 318–320.

Seiden, G., Lipson, S. G. & Franklin, J. 2004 Oscillatory axial banding of particles suspended in a rotating fluid. *Phys. Rev.* E **69** (015301(R)).

Swaminathan, T. N., Mukundakrishnan, K. & Hu, H. H. 2006 Sedimentation of an ellipsoid inside an infinitely long tube at low and intermediate Reynolds numbers. *J. Fluid Mech.* **551**, 357–385.

Wang, Y.-X., Lu, X.-Y. & Zhuang, L.-X. 2004 Numerical analysis of the rotating viscous flow approaching a solid sphere. *Intl J. Numer. Meth. Fluids* **44**, 905–925.